

# Tellurium Transport and Enrichment in Volcanogenic Massive Sulfide Deposits: Numerical Simulations of Vent Fluids and Comparison to Modern Sea-Floor Sulfides

Nicole C. Hurtig,<sup>1,†</sup> Alexander P. Gysi,<sup>1,2</sup> Thomas Monecke,<sup>3</sup> Sven Petersen,<sup>4</sup> and Mark D. Hannington<sup>5</sup>

<sup>1</sup> Department of Earth and Environmental Science, New Mexico Institute of Mining and Technology, 801 Leroy Place, Socorro 87801, New Mexico, USA

<sup>2</sup> New Mexico Bureau of Geology and Mineral Resources, New Mexico Institute of Mining and Technology, 801 Leroy Place, Socorro 87801, New Mexico, USA

<sup>3</sup> Center to Advance the Science of Exploration to Reclamation in Mining, Department of Geology and Geological Engineering, Colorado School of Mines, 1516 Illinois Street, Golden 80401, Colorado, USA

<sup>4</sup>GEOMAR Helmholtz Centre for Ocean Research Kiel, Wischhofstrasse 1-3, 24148 Kiel, Germany

<sup>5</sup> Department of Earth and Environmental Sciences, University of Ottawa, 25 Templeton Street, Ottawa, Ontario K1N 6N5, Canada

#### **Abstract**

Volcanogenic massive sulfide deposits may represent a significant future source of Te, which is a critical element important for the green energy transition. Tellurium is enriched in these settings by up to 10,000 times over its crustal abundance, indicating that fluids in sea-floor hydrothermal systems may transport and precipitate Te. The major element composition of these hydrothermal fluids is controlled by fluid-rock interaction and is well documented based on experimental, modeling, and natural studies; however, controls on Te mobility are still unknown. To better understand Te enrichment in this deposit type, numerical simulations of the mafic-hosted Vienna Woods and the felsic-hosted Fenway sea-floor vents in the Manus basin were performed to predict Te mobility in modern sea-floor hydrothermal vent fluids and Te deposition during sulfide formation. These simulations demonstrate that the mobility of Te in sea-floor hydrothermal systems is primarily controlled by fluid redox and temperature. Tellurium mobility is low in reduced hydrothermal fluids, whereas mobility of this metal is high at oxidized conditions at temperatures above 250°C. Numerical simulations of the reduced vent fluids of the mafic-hosted Vienna Woods site at the back-arc spreading center in the Manus basin yielded Te concentrations as low as 0.2 ppt. In contrast, the more oxidized model fluids of the felsic-hosted Fenway site located on Pual Ridge in the eastern Manus basin contain 50 ppt Te. The models suggest that Te enrichment in these systems reflects rock-buffer control on oxygen fugacity, rather than an enriched source of Te. In fact, the mafic volcanic rocks probably contain more Te than felsic volcanic rocks. The association of elevated Te contents in the felsic-hosted Fenway system likely reflects magmatic volatile input resulting in lower pH and higher  $E_{\rm h}$  of the fluids. More generally, analysis of sulfide samples collected from modern sea-floor vent sites confirms that redox buffering by the host rocks is a first-order control on Te mobility in hydrothermal fluids. The Te content of sulfides from sea-floor hydrothermal vents hosted by basalt-dominated host rocks is generally lower than those of sulfides from vents located in felsic volcanic successions. Literature review suggests that this relationship also holds true for volcanogenic massive sulfides hosted in ancient volcanic successions. Results from reactive transport simulations further suggest that Te deposition during sulfide formation is primarily temperature controlled. Modeling shows that tellurium minerals are coprecipitated with other sulfides at high temperatures (275°-350°C), whereas Te deposition is distinctly lower at intermediate (150°-275°C) and low temperatures (100°-150°C). These predictions agree with geochemical analyses of sea-floor sulfides as Te broadly correlates positively with Cu and Au enrichment in felsic-hosted systems. The findings of this study provide an important baseline for future studies on the behavior of Te in hydrothermal systems and the processes controlling enrichment of this critical mineral in polymetallic sulfide ores.

#### Introduction

Tellurium has a low crustal abundance of 1 ppb Te (McDonough and Sun, 1995) and is considered to be a critical element (Schuyler Anderson, 2018; Fortier et al., 2022). It is primarily (>90%) recovered as a by-product from anode slimes collected from electrolytic refining of porphyry copper ores and used to produce photovoltaic solar cells (Goldfarb et al., 2017; Schuyler Anderson, 2018). Significant primary enrichment of tellurium only occurs in a few ore deposit types, in particular gold deposits where Te-bearing accessory minerals form an important gold host (Goldfarb et al., 2016; Kelley

<sup>†</sup>Corresponding author: e-mail, nicole.hurtig@nmt.edu

and Spry, 2016). One of the world's most important primary tellurium producers is the Kankberg deposit (Åström, 2015), which is located in the Paleoproterozoic Skellefte district of Sweden (Allen et al., 1996). Kankberg is classified as a volcanogenic massive sulfide (VMS deposit), although it shows characteristics that differ from those of other more classical VMS deposits in the district (Åström, 2015; Nordfeldt et al., 2019). The deposit accounts for ~7% of the world's tellurium production of 580 metric tons per year (Boliden, 2021).

Although VMS deposits may represent an important primary source of Te, currently little is known about the processes that control Te enrichment in the polymetallic ores. Recent studies document the occurrence of Te-bearing accessory

minerals in modern sea-floor sulfides (Iizasa et al., 1992, 2019; Lein et al., 2003; Törmänen and Koski, 2005; Fouquet et al., 2010; Berkenbosch et al., 2012; Monecke et al., 2016; Maslennikov et al., 2017; Melekestseva et al., 2017; Firstova et al., 2019) and in black smoker chimney fragments preserved in ancient deposits that have only been overprinted at low metamorphic grades (Novoselov et al., 2006; Vikentyev, 2006; Maslennikov et al., 2009, 2013), providing compelling evidence that Te enrichment in VMS deposits can be syngenetic. However, Te concentrations in modern sea-floor sulfides are highly variable (Monecke et al., 2016), suggesting that multiple factors such as the tectonic setting, the host-rock composition, the vent fluid temperature and chemistry, the degrees of mixing with seawater, and possible phase separation during fluid ascent may be important controls on Te enrichment (Novoselov et al., 2006; Maslennikov et al., 2009, 2013; Monecke et al., 2016; Hassan and Roberts, 2017). Previous work has suggested that enrichment of Te is indicative for a direct magmatic contribution to sea-floor hydrothermal systems (Pilote et al., 2016). The importance of seawater-rock interaction on major element chemistry, pH, and redox of the ore-forming fluids is relatively well established based on comparison of geochemical models with sea-floor vent fluids (Pierre et al., 2018). However, there is still a knowledge gap with regard to Te transport and mobility and the potential use of bulk geochemical data as tracers of these processes.

This study examines the geochemical behavior of Te in modern vent fluids from the mafic-hosted Vienna Woods and the felsic-hosted Fenway sea-floor vents in the Manus basin to identify key controls on Te mobility in hydrothermal fluids and enrichment in sea-floor massive sulfides (Fig. 1).

The speciation of Te in hydrothermal fluids is reviewed. For this purpose, a thermodynamic database of aqueous species and Te-bearing minerals was compiled and implemented in the GEM-Selektor code package (Kulik et al., 2013) and the MINES thermodynamic database (Gysi et al., 2023). Thermodynamic modeling was conducted to determine the solubility behavior of Te, Ag, Au, Cu, Pb, and Zn in heated seawater and hydrothermal vent fluids (Fig. 1). Numerical simulations in GEM-Selektor include Te speciation diagrams, closed- and open-system cooling reactions in fluid conduits, seawater mixing, fluid-rock titration, and the GEM2MT module for 1-D reactive mass transport modeling. Assay data of sulfide samples collected from modern sea-floor hydrothermal vent sites worldwide were compiled to constrain concentration ranges and metal associations in natural systems. Comparisons between the thermodynamic models and the metal associations observed in natural samples from modern sea-floor sulfide occurrences provide new insights into the processes that likely control Te enrichment in VMS deposits.

# Aqueous Tellurium Speciation and Available Experimental Data

Tellurium exists in four different redox states, Te(-II), Te(0), Te(+IV), and Te(+VI), but typically occurs as telluride (-II) and tellurite (+IV) aqueous complexes in natural hydrothermal fluids. Review of the equilibrium constants and speciation of Te at ambient conditions by Filella and May (2019) revealed that many of the reported values are estimates that were derived from Latimer (1938). The solubility of  $\text{TeO}_{2(s)}$  in aqueous fluids has only been determined in two studies at hydrothermal conditions (McPhail, 1995; Grundler et al., 2013).

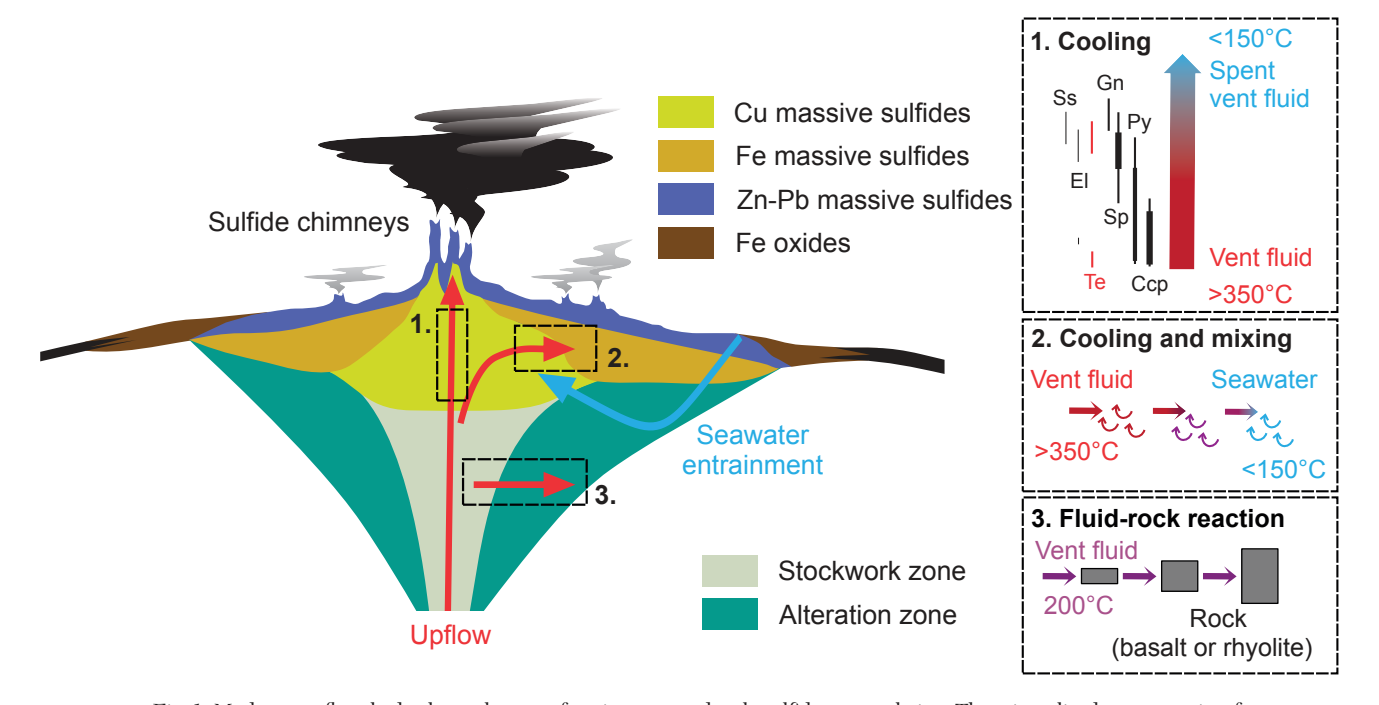


Fig. 1. Modern sea-floor hydrothermal system forming a mound-style sulfide accumulation. The mineralized zones consist of massive Cu, Zn-Pb, and Fe sulfides underlain by a stockwork vein system. The diagram shows key processes occurring at the high-temperature vents that are modeled in this study, including cooling and mineral precipitation from the hot vent fluid, cooling and mixing of the hot vent fluid with entrained seawater, as well as fluid-rock reaction. Mineral abbreviations: Ccp = chalcopyrite, El = electrum, El

McPhail (1995) determined the properties of Te species from  $25^{\circ}$  to  $80^{\circ}$ C using solubility experiments combined with an isocoulombic approach for extrapolation of the data up to  $350^{\circ}$ C. Grundler et al. (2013) identified the Te(+IV) species from TeO<sub>2(s)</sub> solubility experiments and potentiometric measurements up to  $200^{\circ}$ C. They reviewed the occurrence of gaseous Te species, combining solubility experiments in water vapor with previous thermodynamic data (Glemser et al., 1964, 1965, 1966; Barin, 1995; McPhail, 1995).

In this study, thermodynamic data were implemented into GEM-Selektor using log K functions from Grundler et al. (2013) for Te(+IV) species and from McPhail (1995) using a correction value for all other Te species (Table 1). Predicted total Te solubility within the Te(+IV) dominance field shows excellent reproducibility with experimental data reported in Grundler et al. (2013), and corrected log K functions show reproducibility with predicted Gibbs energies of formation for all other Te species reported in McPhail (1995). Detailed information for thermodynamic data evaluation for Te species is provided in the Appendix.

Telluride (-II) includes the species  $Te^{2-}$ ,  $HTe^{-}$ , and  $H_2Te_{(aq)}$ . The existence of  $Te^{2-}$  has been questioned by Marcus (2018), and only limited data exist for the first and second protonation constants. McPhail (1995) determined values for the reaction  $H_2Te_{(aq)}$  to  $HTe^{-} + H^+$ , and derived values for  $H_2Te_{(aq)}$ ,  $HTe^{-}$ , and  $Te^{2-}$ , and a polynuclear  $Te_2^{2-}$  species from the properties of  $H_2Te_{(g)}$  using an isocoulombic approach.

In this contribution,  $Te_2^2$ —was not included in the numerical simulations because the experimental data for this species were only determined at 25°C (Panson, 1963). Unrealistic stability predictions for  $Te_2^2$ —are obtained when using a combination of the updated thermodynamic properties for the  $H_2TeO_{3(aq)}$  species from the experimental data by Grundler et al. (2013) with the equilibrium constant (log K) function presented by McPhail (1995). The recalculated standard Gibbs energy of formation for  $Te_2^2$ —at 25°C would be 12 kJ/mol<sup>-1</sup> lower than the measured value by Panson (1963). Using the updated Gibbs energy of formation, the stability field of  $Te_2^2$ —extends to a pH of ~6 and higher redox conditions at room temperature, whereas polarographic experiments showed that ditelluride dominates only at a pH >12 at reducing conditions

(Panson, 1963). At hydrothermal conditions, the polytelluride species was detected in X-ray absorption spectroscopy experiments by Brugger et al. (2012) in highly reducing fluids (excess NaBH<sub>4(aq)</sub>). Thus, it is possible that the polytelluride species is relevant in hydrothermal fluids; however, at present no reliable thermodynamic data exist to accurately model the stability of this species above 25°C. Additional information for the Te $\frac{1}{2}$  species is available in the Appendix.

Tellurite (+IV) behaves as a triprotic acid in aqueous solution and includes the following species with increasing protonation:  $TeO_3^{2-}$ ,  $HTeO_3^{-}$ ,  $H_2TeO_{3(aq)}$ , and  $H_3TeO_3^{+}$  (or Te(OH)<sub>3</sub>). Grundler et al. (2013) measured the solubility of TeO<sub>2(s)</sub> as a function of pH at 25° to 200°C to determine the (de)protonation of tellurous acid H<sub>2</sub>Te(+IV)O<sub>3(aq)</sub> in combination with potentiometric measurements and nuclear magnetic resonance studies. The study shows that the pK vs. T values plot on a line with constant slope, and therefore that the enthalpy of reaction is constant, which agrees with the assumptions of McPhail (1995). Extended X-ray absorption fine-structure spectroscopic measurements further indicate a threefold coordination, confirming that TeO<sub>3</sub><sup>2-</sup> is the dominant form at high pH, and Te(OH)<sup>†</sup> is the dominant form at low pH (Grundler et al., 2013). Other Te(+IV) species determined at hydrothermal conditions include chloride complexes that have been investigated by Etschmann et al. (2016). This study concluded that chloride complexes are stable only at low pH (≤2 at 25°C) and very high chloride activity (>10 M, i.e., 59 wt % NaCl equivalent), which are not conditions encountered in sea-floor hydrothermal systems. The highestorder chloride complex detected was TeCl<sub>4(aq)</sub> (Etschmann et al., 2016). Other complexes that may form include fluorides, nitrates, sulfates, and sulfides (Barin, 1995; Filella and May, 2019). As consistent thermodynamic data for hydrothermal conditions for these species do not exist yet, these species have not been considered in this study.

Filella and May (2019) showed that tellurate (+VI) occurs as either an oxyanion ( $H_2\text{TeO}_{4(aq)}$ ) or a hydroxide ( $\text{Te}(OH)_{6(aq)}$  or  $H_6\text{TeO}_{6(aq)}$ ). Thermodynamic data for the species  $H_6\text{TeO}_{6(aq)}$ ,  $H_5\text{TeO}_6^-$ , and  $H_4\text{TeO}_6^{2-}$  have been estimated by McPhail (1995). Because tellurate polymerizes at low concentrations and possibly with increased temperature, the determination

Table 1. Logarithm of the Equilibrium Constants of Reaction (K) of Te-Bearing Aqueous Species as a Function of Temperature (°C) at Water Vapor Saturation Pressure ( $P_{sat}$ )

Reaction					$\log K$					
T (°C)	25	50	60	100	150	200	250	300	350	Ref
Te(-II) species										
$H_2 Te_{(aq)} + 1.5O_{2(g)} = H_2 TeO_{3(aq)}$	99.48	90.97	87.93	77.37	66.98	58.83	52.30	47.13	42.92	1
$HTe^- + H^+ + 1.5O_{2(g)} = H_2TeO_{3(aq)}$	102.12	93.68	90.68	80.38	70.41	62.78	56.84	52.32	49.34	1
$Te^{2-} + 2H^+ + 1.5O_{2(g)} = H_2TeO_{3(aq)}$	114.28	105.42	102.26	91.73	81.53	73.96	68.23	64.05	61.77	1
Te(+IV) species										
$TeO_{2(s)} + H_2O = H_2TeO_{3(aq)}$	-4.61	-4.21	-4.07	-3.59	-3.14	-2.77	-2.44	-2.07	-1.53	2
$H_3TeO_{3^+} = H_2TeO_{3(aq)} + \hat{H^+}$	-2.79	-2.43	-2.31	-1.88	-1.46	-1.14	-0.87	-0.62	-0.32	2
$H_2 TeO_{3(aq)} = H TeO_3^- + H^+$	-5.22	-5.57	-5.69	-6.07	-6.39	-6.61	-6.84	-7.17	-7.98	2
$HTeO_3^- = TeO_3^{2-} + H^+$	-10.07	-9.89	-9.83	-9.58	-9.29	-9.04	-8.86	-8.84	-9.25	2
Te(+VI) species										
$H_6 TeO_{6(aq)} = H_2 TeO_{3(aq)} + 2H_2O + 0.5O_{2(g)}$	-2.35	-1.59	-1.31	-0.30	0.74	1.67	2.51	3.33	4.31	1
$H_5TeO_6^- + H^+ = H_2TeO_{3(aq)} + 2H_2O + 0.5O_{2(g)}$	5.35	5.81	6.00	6.71	7.55	8.43	9.36	10.47	12.19	1
$H_4 TeO_6^{2-} + 2H^+ = H_2 TeO_{3(aq)} + 2H_2O + 0.5O_{2(g)}$	16.30	16.39	16.46	16.87	17.60	18.55	19.73	21.31	23.89	1

References: 1 = Updated in this study based on McPhail (1995) see Appendix for more information; 2 = Grundler et al. (2013)

of its equilibrium constants is difficult (Filella and May, 2019). Even though predictions of the stabilities of Te(+VI) species remain uncertain, these species are unlikely to play a significant role in the speciation of natural hydrothermal fluids because they are restricted to highly oxidizing conditions. Even in the study of Grundler et al. (2013), where the redox state of the experimental solutions was buffered by  $TeO_{2(s)}$ , such oxidized Te(+VI) species were not detected.

# Thermodynamic Data for Te Solids

The thermodynamic data of native tellurium, tellurite, and a number of telluride minerals was compiled for this study. However, native tellurium, calaverite, and hessite were the only phases stable in the calculations presented here. Thermodynamic data for Te minerals has not been rigorously evaluated in recent years and for the purpose of this study we largely adopted the standard thermodynamic properties and heat capacity functions from Barin (1995) and volumes from Robie et al. (1967). The thermodynamic data of Te minerals are summarized in Table 2.

All thermodynamic values for native tellurium were taken from Robie and Hemingway (1995). The heat capacity function provided in this study is only valid up to 450°C, which is the melting point of native tellurium. Thermodynamic data for native tellurium are consistent with Barin (1995), who shows an extended heat capacity function and data for the liquid-solid phase transition.

For tellurite (TeO<sub>2</sub>), entropy, heat capacity, Gibbs energy, and the enthalpy of formation were taken from Barin (1995), and the volume was taken from Robie et al. (1967). A recent study by Majzlan et al. (2022) reviewed the enthalpy of tellurite, providing a new recommended value of -322.0 ± 1.3 kJ/mol<sup>-1</sup>, which can be combined with entropy of 70.4 J/mol<sup>-1</sup>/K<sup>-1</sup> from Robie and Hemingway (1995), to calculate an updated Gibbs energy of formation of -267.0 kJ/mol<sup>-1</sup>. This value is within 2.6 kJ of the reported value listed in Barin (1995) and within -2.2 kJ of the value reported in Robie and Hemingway (1995). Because tellurite is used in the  $\log K$  functions determining the thermodynamic properties of the aqueous tellurium species (Table 1), changing tellurite properties would directly affect their stability. Grundler et al. (2013) used the Barin (1995) thermodynamic properties of tellurite and tested the validity of tellurium speciation against their experimental results. Test calculations conducted as part of this study show that Te solubility would change the equilibrium constant by 0.1 log units because of the new thermodynamic data for the tellurite mineral derived by Majzlan et al. (2022), which is within experimental uncertainty reported in the experimental study by Grundler et al. (2013). Therefore, the thermodynamic properties for tellurite listed in Barin (1995) were used in this study to ensure internal consistency of the derived thermodynamic data with the  $\log K$  functions for aqueous species from Grundler et al. (2013).

For altaite and frohbergite, Gibbs energy, enthalpy, heat capacity, and entropy are taken from Barin (1995), and volumes are taken from Robie et al. (1967). The Gibbs energies listed in Barin (1995) are within 2 kJ/mol<sup>-1</sup> compared to the values reported by Robie and Hemingway (1995), which is within uncertainty of calorimetric methods. All thermodynamic data for

Table 2. Thermodynamic Properties of Te-Bearing Minerals

							$\mathrm{C_{p^0}A_0 + A_1 T}$	$+A_2T^{-2}+A_3'$	$\sum_{\rm p}^{\rm p} A_{\rm 0} + A_{\rm 1} T + A_{\rm 2} T^{-2} + A_{\rm 3} T^{-0.5} + A_{\rm 4} T^2 + A_{\rm 5} T^3  ({ m T in}  { m K})$	$T^3$ (T in K)					
		$ ho^t  m Q_t  m G_o$	$\Delta_f \mathrm{H}^\circ$	°S	>		$\mathbf{A}_1$	$A_2$		$A_4$	$A_5$	$\Delta_{\mathrm{trans}} \mathrm{H}^{\circ}$	$\Delta_{\mathrm{trans}} \mathrm{S}^{\circ}$	Τ	
Mineral	Formula	kJmol	$kJ \mod$	Jmol/K	J/bar	$\mathbf{A}_0$	$x10^{-3}$	$x10^{4}$		<sub>9</sub> -01x	$^{6}-01x$	kJ/mol	Jmol/K	O <sub>o</sub>	Ref
Altaite	PbTe	-67.4	9.89-	110.0	4.060	46.77	20.98	-0.508	6.473	-0.281	0.075			25-924	1, 2
Altaite	PbTe	7.69-	-70.7	110.0	4.060	ı	,	ı		1	,	ı	,	25	4
Calaverite	$\mathrm{Au_{0.5}Au_{0.5}Te_2}$	-17.2	-18.6	141.7	4.836	75.33	13.45	25.65		15.06	-5.772	ı	1	25 - 464	, 3 8
Frohbergite	${ m FeTe}_2$	-64.6	-72.4	100.2	3.843	71.91	5.749	-42.35		-0.269	0.063	ı	ı	25-660	1, 2, 4
Fe telluride	${ m FeTe}_{0.9}$	-25.7	-23.2	80.1	3.843	51.44	-2,786	-41.06		-1.027	0.277	ı	ı	25-927	1, 2
Hessite	$Ag_2Te$	-41.6	-36.0	153.6	4.085	71.55	21.04	ı		264.2	-195.8	ı	ı	25 - 148	1, 2
Hessite	$Ag_2Te$	ı	1	1	ı	1,717	-16.33	ı		2,773	-1,071	9.9	15.67	148 - 527	4
Native Te	Te	0.0	0.0	49.7	2.048	19.12	22.06	ı		ı	,	ı	ı	25 - 450	4
Tellurite	${ m TeO}_2$	-269.6	-323.5	74.1	2.775	66.14	13.45	-49.34		0.828	-0.249	ı	1	25 - 1,500	61
Tellurite	${ m TeO}_2$	-264.8	-319.7	70.4	2.775	ı	,	ı		1	,	ı	,	25	4
Vulcanite	CuTe	-26.3	-25.1	9.98	2.704	11.73	18.46	-9.835		-42.47	17.31	ı	ı	25-340	,5 5
Weissite	$\mathrm{Cu}_2\mathrm{Te}$	-47.5	-41.8	134.7	3.882	-131.1	83.87	ı		-4,182	3,697	0.2	0.51	25 - 160	2, 6
Weissite	$\mathrm{Cu}_2\mathrm{Te}$	ı	ı	1	ı	69.13	,	ı		109.9	-74.84	1.9	3.59	160 - 258	61
Weissite	$Cu_2Te$	ı	1	1	ı	113.0	,	ı	1	ı	,	1.0	1.63	258-317	63
Weissite	$\mathrm{Cu}_2\mathrm{Te}$	ı	ı	1	ı	133.9	,	ı	1	1	,	2.4	3.87	317 - 360	61
Weissite	$\mathrm{Cu}_2\mathrm{Te}$	ı	ı	ı	ı	109.5	-18.18	ı		1.458	-0.685	2.0	2.37	360 - 568	61
Zn telluride	ZnTe	-115.3	-119.2	77.8	3.421	44.36	11.68	0.286	-3.949	0.185	-0.049	,	,	25 - 1,027	1, 2

The table lists the standard Gibbs energy of formation ( $\Delta_f G^2$ 298.15K, 1bar) and the standard enthalpy of formation ( $\Delta_f H^2$ 298.15K) from the elements, the absolute entropy ( $S^2$ 298.15K), molar volume ; also shown are the enthalpy ( $\Delta_{trans}$ , H°), entropy ( $\Delta_{trans}$ S°), and temperature range for phase transitions Barin (1995), 3 = Reithmayer et al. (1993), 4 = Robie and Hemingway (1995), 5 = Pertlik (2001), 6 = Bindi et al. (2013) the Cu, Zn, and Ag tellurides are taken from Barin (1995). Echmaeva and Osadchii (2009) experimentally determined the standard thermodynamic data for hessite. They determined a Gibbs energy of formation of  $-40.3~\rm kJ/mol^{-1}$ , which is within  $-1.2~\rm kJ/mol^{-1}$  of the value shown in Barin (1995). Volumes for vulcanite are taken from Pertlik (2001), for weissite from Bindi et al. (2013), and for Zn telluride and hessite from Robie et al. (1967). Thermodynamic data for calaverite are taken from Barin (1995) and volumes from Reithmayer et al. (1993).

#### Chemical Composition of Sea-Floor Massive Sulfides

To constrain the geochemical behavior of Te in sea-floor hydrothermal systems, a database of bulk geochemical analyses of sea-floor sulfides was compiled. This database is based on Hannington et al. (1994, 2005, 2010) as well as Monecke et al. (2016). The database was filtered for hydrothermal vent sites located at basalt-hosted mid-ocean ridges and mature back-arc spreading centers as well as vent sites occurring in arc-related rifts, which include the felsic-hosted vent sites of the eastern Manus basin. In total, assay data were compiled for 1,159 samples of massive sea-floor sulfides (App. Tables A4 and A5). For this study, the compiled data were further filtered using Cu + Fe + Pb + Zn >30% to ensure that only samples containing a high proportion of sulfides are included in the statistical analysis. Of these data, a total of 504 samples have Te concentrations above the limit of detection (Table 3).

#### Tellurium content of sea-floor massive sulfides

Sulfide samples collected from mafic- and felsic-dominated vent sites on the modern sea floor overall have Te concentrations averaging 8.8 ppm with a median concentration of 0.9 ppm (Table 3; App. Table A4). Sea-floor sulfides from basalthosted midocean ridges have lower average Te concentrations of 3.6 ppm (n=224) compared to those from rifted arcs, which average 13.0 ppm Te (n=275). Sulfides from back-arc spreading centers have an average of 6.5 ppm Te. However, this latter data set only contains five analyses from the Lau basin. Amongst sulfide samples from basalt-hosted mid-ocean ridges, those from the Mid-Atlantic Ridge (n=30) and the Alarcon Rise (n=2) have the highest average Te concentra-

tions at 10.0 and 16.0 ppm, respectively. The highest Te concentration of 164 ppm was measured in a sample from Juan de Fuca Ridge. Sulfide samples from rifted arcs generally have high average Te concentrations. This includes samples from the Okinawa Trough (n=20) and the Manus basin (n=251) with average Te concentrations of 36.5 and 11.3 ppm as well as maximum Te concentrations of 230 and 431 ppm, respectively. Compared to the crustal average concentrations of 1 ppb Te (McDonough and Sun, 1995), modern sea-floor massive sulfides show a Te enrichment factor of 1,000 to 10,000.

Sea-floor massive sulfides from felsic-hosted rifted arcs generally have higher median and average concentrations of Te, Au, Ag, Cu, and Pb compared to sulfides from basalt-hosted mid-ocean ridges (Fig. 2), whereas Zn concentrations are similar for samples from both settings (Fig. 2b). These trends suggest that Te as well as the base and precious metals are generally enriched in sea-floor sulfides hosted by felsic volcanic successions formed in rifted arcs.

#### Elemental correlations

Statistical evaluations were conducted using IoGAS v7.4.2 software package. Element correlations of Te with base and precious metals are below significant Pearson's correlation coefficients (i.e., values are <0.3 to >-0.3). In general, Te correlates positively with Ag, Cu, and Pb and negatively with Fe (Table 4). In samples from basalt-hosted mid-ocean ridges, Te only correlates positively with Ag. In sulfides from back-arc spreading centers, Te correlates positively with Au, to a lesser extent with Ag, Zn, Pb, and Cu, and correlates negatively with Fe. In samples from rifted arcs, Te correlates positively with Cu, Pb, and Zn and negatively with Fe.

The Cu/Ag ratio provides important insights into the conditions of sea-floor sulfide formation and will subsequently be tied in with numerical simulations (Fig. 3). This ratio reflects the temperature of sulfide formation, as Cu is generally enriched in high-temperature sulfides containing chalcopyrite, whereas Ag is more commonly enriched at lower temperatures in sulfides containing sulfosalts, sphalerite, and galena (Hannington et al., 2005). In the geochemical analyses from the modern sea floor, Te and Fe correlate positively with the Cu/Ag ratio (Fig. 3a, b), whereas Pb and Zn correlate nega-

Table 3. Statistical Analyses of Te Data From Modern Sea-Floor Sulfide Samples

					Standard	
Te ppm	n	Minimum	Maximum	Average	deviation	Median
All data	504	0.01	431	8.77	28.7	0.85
Basalt-hosted mid-ocean ridges	224	0.02	164	3.63	13.3	0.60
East Pacific Rise	40	0.02	8.00	1.19	1.91	0.28
Pacific-Antarctic Ridge	2	0.20	0.50	0.35	0.21	0.35
Juan de Fuca Ridge	120	0.10	164	2.73	16.1	0.60
Central Indian Ridge	8	0.60	2.50	1.78	0.74	2.05
Galapagos rift	22	0.20	17.0	4.14	5.76	0.95
Mid-Atlantic Ridge	30	0.03	61.2	9.99	13.9	2.88
Alarcon Rise	2	14.0	18.0	16.0	2.83	16.0
Back-arc spreading centers	5	5.40	7.90	6.52	1.10	6.50
Lau basin	5	5.40	7.90	6.52	1.10	6.50
Rifted arcs	275	0.01	431	13.0	36.4	2.00
Vate Trough	0					
Bransfield Strait	4	0.20	0.60	0.33	0.19	0.25
Manus basin	251	0.01	431	11.3	33.2	2.00
Okinawa Trough	20	0.18	230	36.5	62.9	12.4

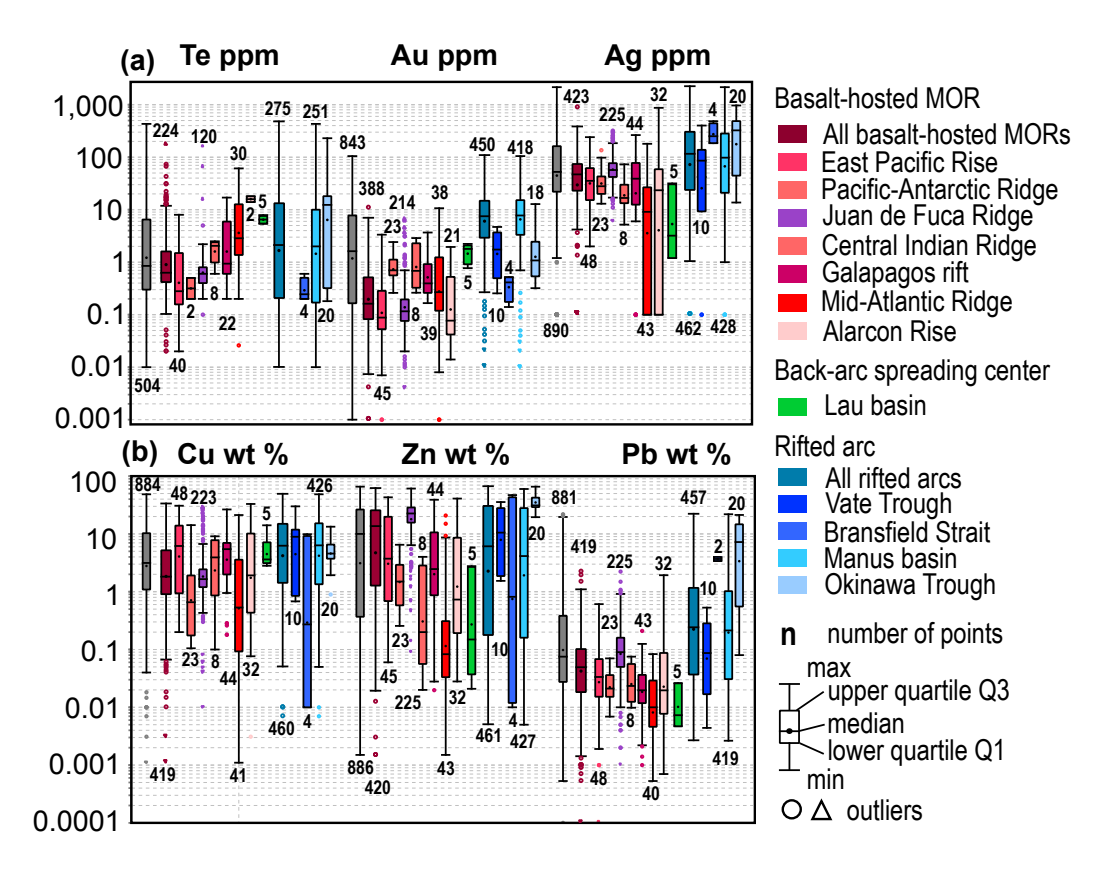


Fig. 2. Box-and-whisker diagrams of elemental concentrations measured in sulfide samples collected from sea-floor hydrothermal vents located in different tectonic settings (modified from Monecke et al., 2016). a) Te, Au, and Ag concentrations. b) Cu, Zn, and Pb concentrations. Data are filtered to Cu + Fe + Pb + Zn > 30%. See Appendix Table A4 for summary statistics. Gray bars are values for all data and black circles are geometric mean values. MOR = mid-ocean ridge.

Table 4. Pearson Correlation Coefficients for Assay Data Obtained on Modern Sea-Floor Sulfide Samples

	All data (n = 504)	Basalt-hosted mid-ocean ridges (n = 224)	Back-arc spreading centers (n = 5)	Rifted arcs $(n = 275)$
Au ppm	0.01	0.04	0.90	-0.08
Ag ppm	0.12	0.18	0.62	0.09
Cu wt %	0.16	0.05	0.40	0.15
Fe wt %	-0.11	-0.04	-0.74	-0.12
Pb wt %	0.27	-0.01	0.62	0.26
Zn wt $\%$	0.02	0.001	0.60	0.10

tively with the Cu/Ag ratio (Fig. 3c, d). The positive correlation of Te with the Cu/Ag ratios is better developed in the samples collected from vents hosted in mafic rocks when compared to those from felsic-hosted vents (Fig. 3a). Sulfides from the Okinawa Trough show a negative correlation of Te with the Cu/Ag ratio, whereas the large data set from the Manus basin shows a positive correlation of Te with the Cu/Ag ratio. The Fe contents of massive sulfides are generally higher in samples from basalt-hosted vent sites compared to those from vents located in rifted arcs (Fig. 3b). Gold, Pb, and Zn show higher concentrations in the samples from felsic-hosted vents, with Pb and Zn correlating negatively with the Cu/Ag

ratio (Fig. 3c-e). Zinc shows a change in slope at a Cu/Ag ratio of around 2,000, indicating a sharp drop-off in Zn contents in the Cu-rich parts of the sulfide occurrences (Fig. 3c). Sulfides from the Okinawa Trough show a positive correlation of Zn with the Cu/Ag ratio. Gold correlates negatively with Cu/Ag in sea-floor massive sulfides from basalt-hosted vents. Samples from the rifted arcs show a weak positive correlation of Au with Cu/Ag below a ratio of 2,000 and a negative correlation above Cu/Ag values of 2,000 (Fig. 3e).

#### **Numerical Modeling**

#### Methodology

Numerical modeling was carried out in the Na-K-Ca-Fe-Mg-Al-Si-Cl-S-C-O-H thermodynamic system containing Te and precious/base metals (Ag, Au, Cu, Fe, Pb, and Zn) using the GEM-Selektor code package (Kulik et al., 2013). Thermodynamic data for minerals and aqueous species were taken from the MINES thermodynamic database (Gysi et al., 2023; https://geoinfo.nmt.edu/mines-tdb). Thermodynamic properties for Ag (Akinfiev and Zotov, 2001, 2010), Au (Akinfiev and Zotov, 2001, 2010; Stefánsson and Seward, 2003a, b), Cu (Akinfiev and Zotov, 2001, 2010; Liu and McPhail, 2005; Brugger et al., 2007), Pb (Shock et al., 1997; Sverjensky et al., 1997), and Zn (Akinfiev and Tagirov, 2014; Mei et al., 2015) were recently added to the database. De-

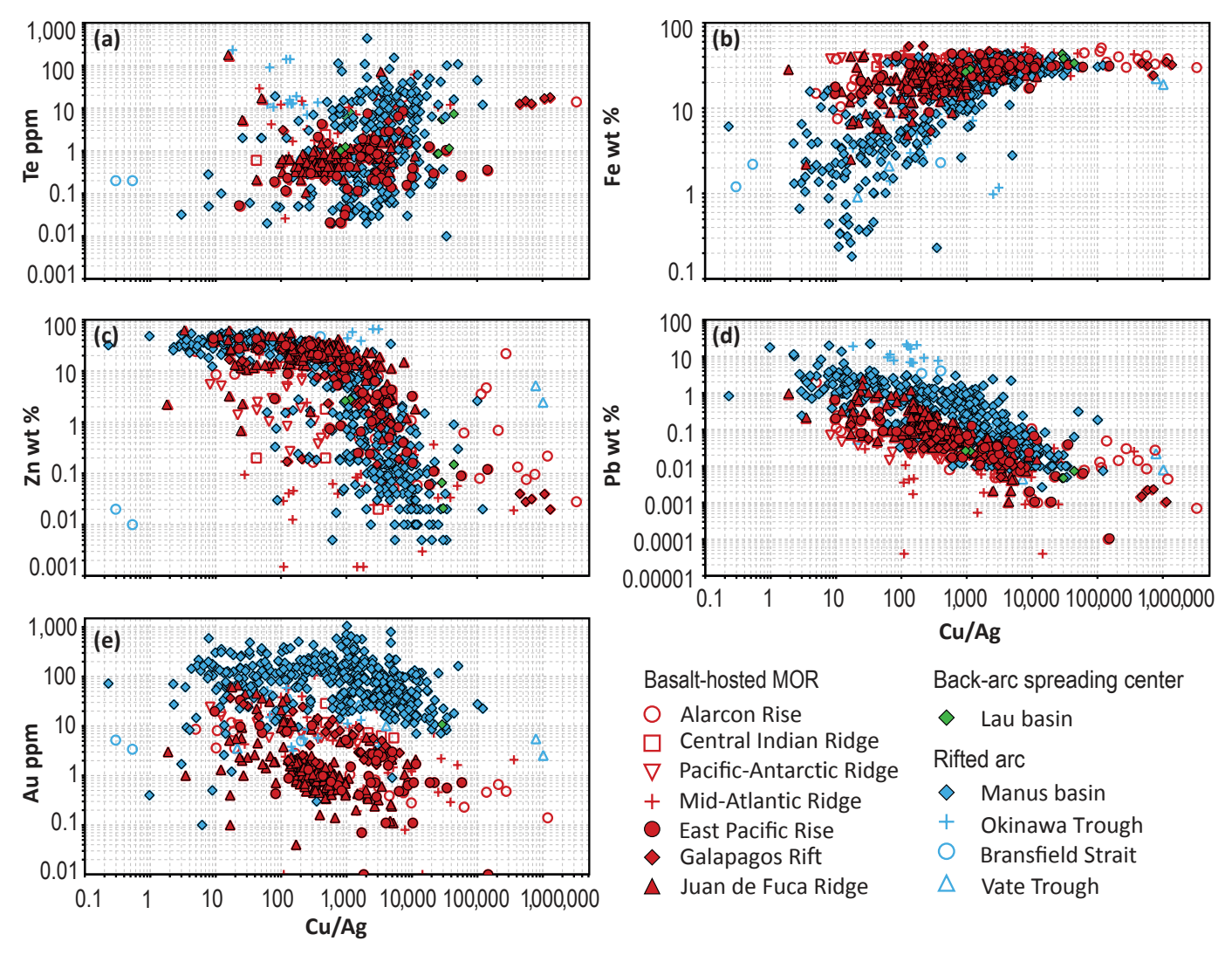


Fig. 3. Composition of sulfide samples collected from sea-floor hydrothermal vents located in different tectonic settings. Elements are plotted as a function of the Cu/Ag ratio (in ppm), which is a proxy for the temperature of sulfide formation with higher Cu/Ag ratios indicating high temperatures. MOR = mid-ocean ridge.

tailed references for individual species are summarized in Appendix Table A3. Thermodynamic properties for Te are summarized in Tables 1 and 2. The TSolMod library was used to retrieve equations of state and activity models (Wagner et al., 2012). The thermodynamic properties for aqueous species were calculated at the temperature and pressure of interest using the revised HKF (Helgeson-Kirkham-Flowers) equation-of-state (Helgeson et al., 1981; Shock and Helgeson, 1988; Tanger and Helgeson, 1988; Shock et al., 1992; Johnson et al., 1992). A standard state of unit activity was adopted for pure H<sub>2</sub>O and for the aqueous species in a hypothetical 1 molal solution referenced at infinite dilution for any temperature and pressure. The activity coefficients  $(\gamma_i)$ for the aqueous species were calculated using the extended Debye-Hückel equation (Robinson and Stokes, 1968) assuming NaCl as the background electrolyte (Helgeson and Kirkham, 1974; Helgeson et al., 1981). Arsenic, Bi, Sb, and Se were not considered for modeling in this study, thereby restricting the considered Te minerals to altaite, calaverite,

hessite, native tellurium, tellurite, Fe telluride, Zn telluride, vulcanite, and weissite, for which thermodynamic data are available in the literature (Table 2).

#### Te oxidation states and speciation in seawater

Numerical simulations were conducted to determine the Te oxidation states and the stability of aqueous Te species in heated seawater as a function of pH, redox, and temperature using the updated thermodynamic data set (Tables 1 and 2). The calculations were conducted to delineate which Te species are likely relevant for the solubility of Te in heated seawater and to be able to compare the results with the speciation of Te in hydrothermal vent fluids of known compositions. Heated seawater is significantly more oxidizing than rock-buffered hydrothermal vent fluids, therefore these simulations provide an important end member to understand Te speciation in seafloor hydrothermal systems.

The seawater composition (Table 5) used in the calculations was taken from Millero et al. (2008) as modified by Pierre et

al. (2018). The initial redox potential ( $E_{\rm h}$  in V, relative to a standard hydrogen electrode) was varied to bracket  $E_{\rm h}$  values of 0.045 V and -0.235 V at 25°C and 1 bar, while maintaining equilibrium with native Te(s). These  $E_{\rm h}$  values are within the range for oxidized surface (0.55–0.73 V) and anoxic (-0.27 V) seawater, respectively (Millero, 1977). Table 5 lists the calculated total dissolved Te concentrations in heated seawater, ranging from <1 ppq in anoxic seawater at 25°C to 1.9 ppm Te in oxidized seawater at 350°C, indicating a strong dependence on the redox potential. At oxidizing conditions ( $E_{\rm h}=0.045$  V;  $\log f_{\rm O_2}=-49.9$ ), Te is several orders of magnitude more soluble compared to its solubility in reduced seawater ( $E_{\rm h}=-0.235$  V;  $\log f_{\rm O_2}=-68.9$ ), independent of the equilibration temperature.

Tellurium species predominance fields are shown in Figure 4 as a function of temperature at 100°, 250°, and 350°C. The calculations indicate that Te(-II) and Te(+IV) species predominate in seawater, whereas the Te(+VI) species are only stable in highly oxidizing fluids with calculated  $f_{\rm O_9}$  values >0. Major Te species include HTeO3 and HTe in heated seawater at 100 °C, whereas the  $H_2$ TeO<sub>3(aq)</sub> species is predominant at 250 ° and 350°C. The calculated species predominance diagrams also show that by heating seawater from 100° to 350°C, the dominant Te(+IV) species vary from H<sub>2</sub>TeO<sub>3(aq)</sub> and HTeO<sub>3</sub> toward an increase of the stability fields of H<sub>2</sub>TeO<sub>3(aq)</sub> and  $TeO_3^{2-}$  and a decrease of the stability field of HTeO<sub>3</sub>. At more reducing conditions, the dominant Te(-II) species shifts with increasing temperatures from HTe<sup>-</sup> to H<sub>2</sub>Te<sub>(aq)</sub> and HTe<sup>-</sup>. The species Te<sup>2-</sup> is only predicted to be stable at high pH values. In rock-buffered hydrothermal fluids, HTe<sup>-</sup>, H<sub>2</sub>Te<sub>(aq)</sub>, and H<sub>2</sub>TeO<sub>3(aq)</sub> predominate at high temperatures at pH values of 4 to 7 and redox conditions between the hematite-magnetite and quartz-fayalite-magnetite buffers (Fig. 4).

Figure 5 shows a series of speciation diagrams illustrating the stability of the different Te(-II) and Te(+IV) species as a function of pH in heated seawater at 250° and 350°C. The calculations show that the Te(+IV) species dominate in heated oxidized seawater and that the total dissolved Te concentration in the fluid is independent of pH at 250°C. At 350°C, the predicted Te concentrations increase from 1.8 ppm at neutral pH to 52 ppm Te at pH values below 4 due to an increased stability of the H<sub>3</sub>TeO<sub>3</sub> species. In contrast, seawater under anoxic conditions displays a much lower Te solubility, which strongly depends on pH. At 350°C, the Te solubility decreases from 52 ppm Te at low pH to ~0.01 ppb Te at neutral conditions and increases again to 0.2 ppm Te at alkaline pH. The predicted Te(+IV) species are dominant at pH values below 6, and Te(-II) species (particularly HTe<sup>-</sup>) become important at pH values >6. The total dissolved Te concentrations can reach similar values of 52 ppm Te between oxidized and reduced seawater at temperatures of 350°C at low pH.

#### Te behavior in hydrothermal fluids

In addition to heated seawater, the behavior of Te in hydrothermal vent fluids was modeled. To account for host-rock controls on vent fluid composition, this study used data collected at two well-studied vent sites in the Manus back-arc basin in Papua New Guinea, situated 150 km apart (Reeves et al., 2011):

Table 5. Composition of Seawater (modified from Millero et al., 2008) and Calculated pH,  $E_{\rm h}$  (V),  $\log f_{\rm O_2}$  (bar), and Total Te Solubility of Heated Seawater at Temperatures Ranging From 25° to 350°C

Seawater			
pH <sub>25°C,1 bar</sub>	8.1		
Na	0.469 mol/kg		
K	0.0102 mol/kg		
Ca	0.0104 mol/kg		
Mg	0.0528 mol/kg		
Cl	0.5467 mol/kg		
S	0.0282 mol/kg		
$CO_2$	0.0020  mol/kg		
Te solubility	$Oxidized^1$	Anoxic <sup>2</sup>	Eq min <sup>3</sup>
T = 25°C, $P = 1$ bar			
pН	7.5	7.5	Dol
$E_{\rm h}$ (V)	0.045	-0.235	
$\log f_{\mathrm{O}_2}$ (bar)	-49.9	-68.9	
Te (mol/kg) <sup>4</sup>	$1.44\times10^{-5}$	$4.39\times10^{-18}$	
T = 100°C, $P = 200$ bar			
pH	6.6	6.6	Dol
$E_{\rm h}\left({ m V}\right)$	0.031	-0.241	1501
$\log f_{\rm O_2}$ (bar)	-37.8	-52.6	
Te (mol/kg) <sup>4</sup>	$1.44 \times 10^{-5}$	$7.39 \times 10^{-16}$	
10 (11101/115)	1.11 // 10	1.55 X 15	
$T = 250^{\circ}C$ , $P = 200 \text{ bar}$			
pН	5.8	5.8	Anh, Bre
$E_{\rm h}\left({ m V} ight)$	-0.051	-0.267	
$\log f_{\mathrm{O}_2}$ (bar)	-25.4	-33.7	
Te (mol/kg) <sup>4</sup>	$1.44\times10^{-5}$	$1.09\times10^{-13}$	
T = 350°C, $P = 200$ bar			
pH	5.6	5.6	Anh, Bre
$E_{\rm h}({ m V})$	-0.124	-0.257	min, Dic
	-0.124 -21.1	-0.257 -25.4	
$\log f_{\mathrm{O_2}}  \mathrm{(bar)}$ Te (mol/kg) <sup>4</sup>	$1.45 \times 10^{-5}$	$7.37 \times 10^{-10}$	
10 (11101) 185/	1.10 \ 10	1.01 × 10	

Abbreviations: Anh = anhydrite, Brc = brucite, Dol = dolomite

- $^{1}$  0.001 g  $O_{2}$  added
- <sup>2</sup> No O<sub>2</sub> added
- <sup>3</sup> Equilibrated minerals
- <sup>4</sup> Total dissolved Te in equilibrium with native Te
- 1. The Vienna Woods basalt-hosted hydrothermal vent field, which is located at the Manus back-arc spreading center at a depth of ~2,500 m and which displays high-temperature venting at 273° to 285°C; and
- 2. The dacite- to rhyodacite-hosted Fenway hydrothermal vent field, which forms part of the PACMANUS area on Pual Ridge in the eastern Manus basin. Felsic volcanism along Pual Ridge is related to rifting. The Fenway vent field is located at a depth of ~1,700 m, with high-temperature venting occurring at 329° to 358°C.

The measured vent fluid compositions and the inputs used for the two models are listed in Table 6. In both cases, the highest-temperature vent fluid compositions analyzed by Reeves et al. (2011) were selected. Fluid sampling at different locations within each vent field by Reeves et al. (2011) suggested that variability in the vent fluid compositions is limited. Selection of a different vent fluid composition from the data set presented by Reeves et al. (2011) would not significantly affect the modeling performed here.

To obtain model input fluid compositions for the titration and sequential reactor simulations of this study, the measured

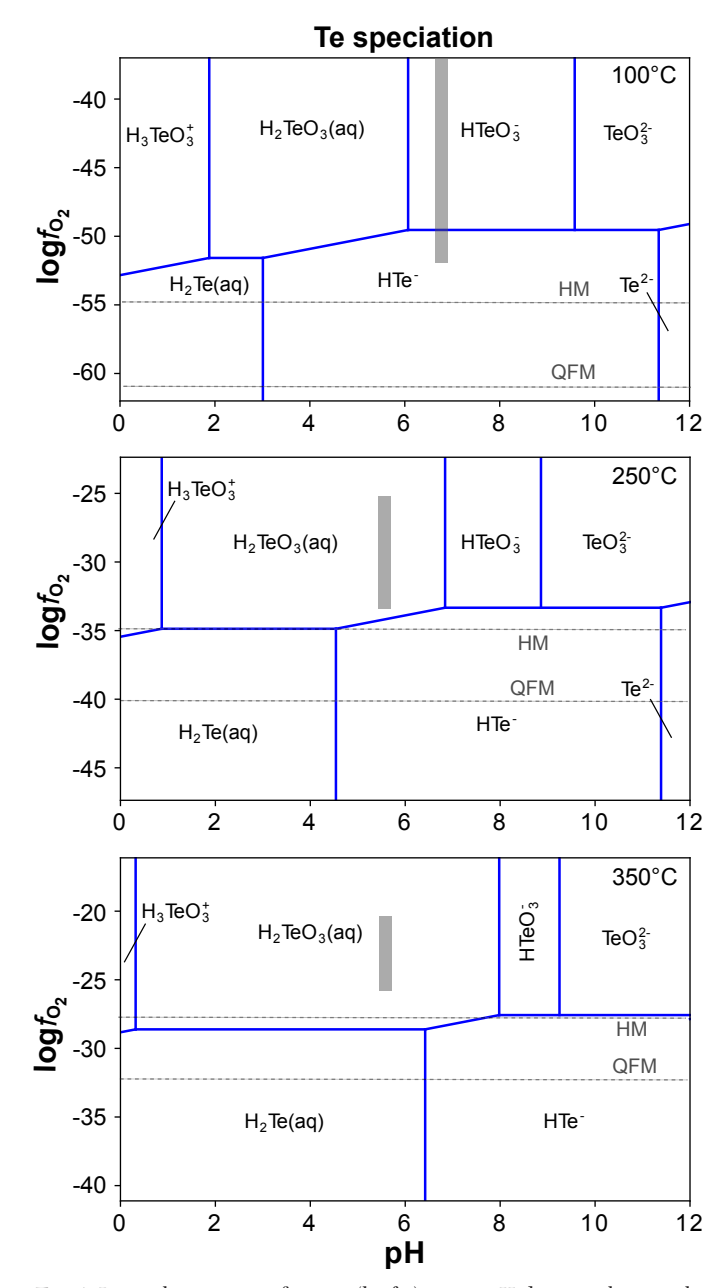


Fig. 4. Logarithmic oxygen fugacity  $(\log f_{\rm O_2})$  versus pH diagram showing the predominance of Te aqueous species in heated seawater at 100°, 250°, and 350°C. Speciation was calculated at saturated water vapor pressure based on the thermodynamic data listed in Tables 1 and 2. The gray bar indicates the range of values for heated seawater listed in Table 5. The dotted lines show the quartz-fayalite-magnetite (QFM) and hematite-magnetite (HM) buffers, which provide lower and upper boundaries for the redox conditions encountered in most hydrothermal fluids, respectively.

vent fluids were initially equilibrated at  $25^{\circ}$ C and 1 bar by iteratively varying redox potential (i.e.,  $O_2$  and  $H_2$  content) and the HCl concentration to achieve the measured pH and S(-II)/S(+IV) speciation balance according to the measured fluid compositions from Reeves et al. (2011). This was followed by equilibration at  $350^{\circ}$ C and 280 bar for the Vienna Woods fluid and 200 bar for the Fenway fluid, allowing for saturated phases to precipitate out. The conditions of the high-temperature equilibration were the starting conditions

for the subsequent cooling and mixing models. The Vienna Woods fluid was saturated with respect to anhydrite, chlorite, and clinopyroxene, which slightly limited the concentrations of Al, Ca, Fe, S, and Si in the model input fluid (Table 6). The Fenway fluid showed saturation with anhydrite and pyrite resulting in slightly lower Ca, S, and Fe concentrations in the Fenway model input fluid compared to the concentrations measured in the hydrothermal vent fluid (Table 6).

Metal (Ag, Au, Cu, Pb, Te, and Zn) concentrations were not reported for the vent fluids by Reeves et al. (2011). Therefore, the model input fluids were equilibrated with an assemblage of chalcopyrite, galena, native gold, native tellurium, native silver, and sphalerite to predict metal solubility in the model input fluids. These calculations were performed at 350°C assuming a pressure of 280 bar for the Vienna Woods and 200 bar for the Fenway model vent fluids. Similar to the above calculations, the selected pressures are slightly higher than the hydrostatic pressures at the vent sites to account for the fact that metal precipitation likely commences below the sea floor and to ensure stability of the numerical simulation using the revised HKF equation-of-state by restricting conditions to those of the liquid field of the NaCl-H<sub>2</sub>O system (Driesner and Heinrich, 2007). This way, complications arising from boiling of the vent fluids and/or separation of a CO<sub>2</sub>-H<sub>2</sub>S-rich vapor phase were avoided. As a final step, the redox potential of the two model vent fluids was modified again until the pH and  $E_{\rm h}$  of the model input fluids matched the values of the heated fluid from the metal-free model as a simulation constraint. These preparatory steps are necessary as the GEM-Selektor code package does not operate using fixed redox buffer pairs but calculates pH and  $E_h$  by the Gibbs energy minimization method.

Redox titration models (i.e., addition of H<sub>2</sub> and O<sub>2</sub>) were performed to determine the metal solubility and aqueous Te speciation for a range of pH and  $E_h$  conditions for both model input fluid compositions (Fig. 6). The simulations show that the Vienna Woods model input fluid is more reduced than the Fenway model input fluid. The Fenway model input fluid has a low pH value of ~3 to 4. Consequently, the Fenway model input fluid has overall higher metal solubility. Tellurium solubility strongly depends on redox conditions and increases by ~7 orders of magnitude between  $E_h$  values of -0.26 V (log  $f_{O_2}$ = -30) to +0.2 V (log  $f_{O_2}$  = -21). The simulations also indicate that H<sub>2</sub>TeO<sub>3(aq)</sub> controls Te solubility in both model input fluids. For reference, the pH and  $E_h$  of heated seawater from this study and heated seawater equilibrated with basaltic rocks at high temperatures (Pierre et al., 2018) are shown in Figure 6. The logarithmic oxygen fugacity of oxidized seawater is -21.1 and that of anoxic seawater is -25.4 (Table 5), in comparison to much lower values of partially rock-equilibrated fluids such as -29.9 for the Vienna Woods and -27.4 for Fenway model input fluids (Table 6). The pH and  $E_h$  covary, forming diagonal trends for fluids of the same composition. The Vienna Woods model input fluid has a composition consistent with seawater that has extensively interacted with basaltic rocks at high temperatures (Fig. 6). The  $E_h$  value below -0.2 V indicates that interaction of the seawater with basaltic rocks occurred at rock-buffered conditions (cf. Pierre et al., 2018). The Fenway model input fluid, on the other hand, is farther to the right of the gray box outlining rock-equilibrated

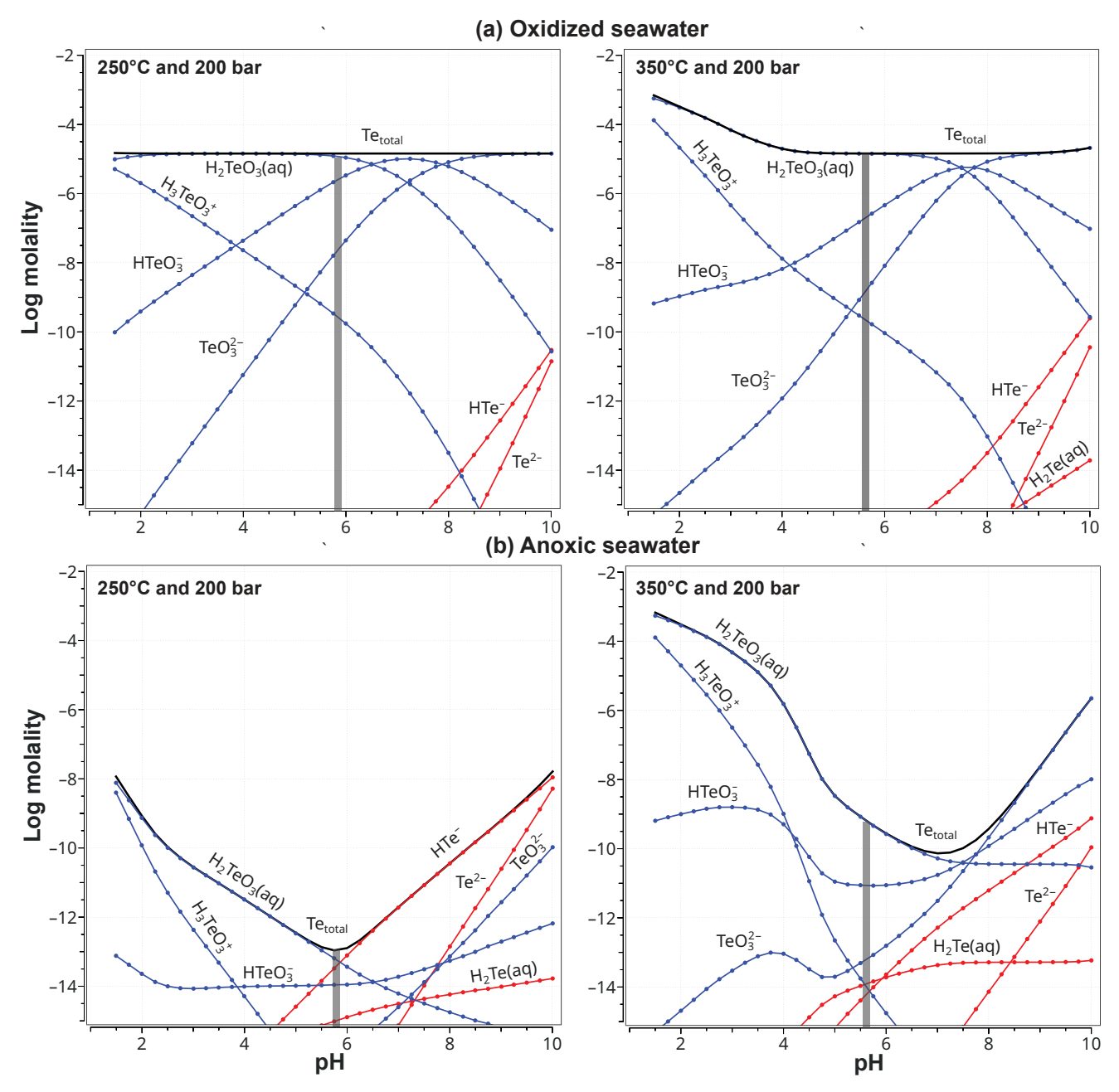


Fig. 5. Calculated total Te solubility ( $Te_{total}$ ) and logarithm of Te species molality as a function of pH in heated seawater at 250° and 350°C at 200 bar in equilibrium with native  $Te_{(s)}$ . a) Calculation using oxidized seawater with an initial pH value of 7.5 and  $E_h$  of 0.045 V, which is equivalent to a  $\log f_{0_2}$  value of -68.9 at 25°C and 1 bar. b) Calculations using anoxic seawater with an initial pH value of 7.5 and  $E_h$  of -0.235 V, which is equivalent to a  $\log f_{0_2}$  value of -49.9 at 25°C and 1 bar. The gray bar indicates the range of values for heated seawater listed in Table 5.

vent fluid compositions (Fig. 6a, b). This indicates that the Fenway fluid has not fully equilibrated with the wall rocks, presumably because felsic rocks have a lower buffering capacity than mafic rocks (Gysi and Stefánsson, 2012; Gysi, 2017; Pierre et al., 2018). Redox buffering through fluid-rock reaction mainly depends on the amount of Fe and its oxidation state. Therefore, mafic rocks more strongly affect redox conditions of vent fluids when compared to Fe-poor felsic rocks. Furthermore, the difference in pH between the two fluids may be related to the presence of magmatic volatiles

(HCl,  $H_2S$ , and  $CO_2$ ) in the Fenway fluids as suggested by Reeves et al. (2011).

#### Fluid-rock reaction models

To evaluate the effect of fluid-rock reaction on metal solubility in vent fluids, two rock titration models were conducted adding 0 to 500 g of basalt or rhyolite to 1 kg of the Fenway model input fluid at 200°C and 200 bar (Fig. 7). Basaltic glass from Gysi and Stefánsson (2011) and rhyolitic glass from Bailey et al. (1989) were selected as representative rock compositions

Table 6. Measured Hydrothermal Vent Fluid Compositions for Vienna Woods and Fenway from
Reeves et al. (2011) and Calculated Model Input Compositions for the Two Vent Sites

	Measured vent flu	id compositions		Model input c	omposition
	Vienna Woods	Fenway		Vienna Woods	Fenway
Depth (m)	2,500	1,700	Depth (m)	2,500	1,700
T (°C)	285	358	T (°C)	350	350
P (bar)	255	167	P (bar)	280	200
pH <sub>25°C,1 bar</sub>	4.7	2.7	pH <sub>25°C,1 bar</sub>	4.7	2.7
			$pH_{T,P}$	5.1	3.9
			$E_{ m h}$	-0.26	-0.04
			$\log f_{O_2}$	-29.9	-27.4
Mg (mol/kg)	$1.11 \times 10^{-3}$	$4.52 \times 10^{-3}$	Ag (mol/kg)	$4.92 \times 10^{-6}$	$1.69 \times 10^{-4}$
Na	$5.04 \times 10^{-1}$	$4.17 \times 10^{-1}$	Al	$2.09 \times 10^{-6}$	$6.04 \times 10^{-6}$
Cl	$6.63 \times 10^{-1}$	$5.89 \times 10^{-1}$	Au	$1.90 \times 10^{-7}$	$6.30 \times 10^{-7}$
Ca	$6.95 \times 10^{-2}$	$2.22 \times 10^{-2}$	C	$4.57 \times 10^{-3}$	$4.43 \times 10^{-2}$
K	$2.00 \times 10^{-2}$	$7.39 \times 10^{-2}$	Ca	$5.13 \times 10^{-2}$	$2.89 \times 10^{-4}$
$SiO_2$	$1.44 \times 10^{-2}$	$1.19 \times 10^{-2}$	Cl	$6.55 \times 10^{-1}$	$5.52 \times 10^{-1}$
$SO_4^{2-}$	$8.70 \times 10^{-4}$	$9.70 \times 10^{-4}$	Cu	$5.25 \times 10^{-5}$	$5.39 \times 10^{-4}$
F	$1.90 \times 10^{-5}$	$1.65 \times 10^{-4}$	F	$1.88 \times 10^{-5}$	$1.64 \times 10^{-4}$
Fe	$1.27 \times 10^{-4}$	$1.15 \times 10^{-2}$	Fe	$1.11 \times 10^{-4}$	$1.48 \times 10^{-2}$
Al	$6.70 \times 10^{-6}$	$6.10 \times 10^{-6}$	K	$1.98 \times 10^{-2}$	$7.32 \times 10^{-2}$
$H_2S$	$1.53 \times 10^{-3}$	$1.52 \times 10^{-2}$	Mg	$8.91 \times 10^{-4}$	$4.48 \times 10^{-3}$
$CO_2$	$4.55 \times 10^{-3}$	$4.46 \times 10^{-2}$	Na	$4.99 \times 10^{-1}$	$4.13 \times 10^{-1}$
$H_2$	$4.38 \times 10^{-5}$	$2.36 \times 10^{-4}$	Pb	$2.14 \times 10^{-4}$	$8.66 \times 10^{-3}$
$CH_4$	$6.31 \times 10^{-5}$	$3.25 \times 10^{-5}$	S	$2.97 \times 10^{-3}$	$3.07 \times 10^{-2}$
CO	-	$1.42 \times 10^{-7}$	Si	$1.22 \times 10^{-2}$	$1.18 \times 10^{-2}$
			Te	$1.48 \times 10^{-12}$	$3.55 \times 10^{-10}$
			Zn	$1.55 \times 10^{-2}$	$2.13 \times 10^{-2}$
			Sat min <sup>1</sup>	Anh, Cpx, Chl	Anh, Py

Abbreviations: Anh = anhydrite, Chl = chlorite, Cpx = clinopyroxene, Py = pyrite

for the simulations. Both glasses contain dominantly Fe2+ acting as a reducing agent during fluid-rock reaction. After adding  $\sim 50$  g of rock, the pH increased and the  $E_h$  decreased to rock-buffered conditions (Fig. 7a, b). The model shows that the fluid equilibrated with basalt has a higher pH and lower  $E_{\rm h}$  (i.e., more reducing) compared to the fluid equilibrated with rhyolite (Fig. 7a, b). Metal solubility generally decreases with increasing fluid-rock reaction in both models, indicating limited metal mobility in rock-equilibrated fluids. Gold solubility initially decreases in both models and increases again in the basalt titration model at rock-equilibrated conditions. Tellurium solubility generally decreases with increasing fluidrock reaction in both models (Fig. 7c, d). In the basalt-equilibrated model, Te solubility initially decreases ~6 orders of magnitude until rock buffering is achieved and then increases again by ~2 orders of magnitude. However, Te is not considered mobile below 250°C, as discussed in the cooling models below. Alteration in the mafic simulation consists of quartzfeldspar-chlorite-muscovite-titanite-calcite (Fig. 7e), and in the felsic simulation it consists of quartz-feldspar-muscovitecalcite-anhydrite-hematite-rutile-chlorite (Fig. 7f). Chlorite is more prevalent in the mafic simulation, whereas the felsic simulation shows larger amounts of quartz, microcline, muscovite, and hematite. Epidote starts to form above 250°C and becomes more prevalent with increasing temperature. The alteration assemblages can be subdivided into three distinct zones, which are (1) the pyrite-quartz vein zone, (2) the vein alteration halo showing quartz-muscovite ± anhydrite ± hematite  $\pm$  chlorite, and (3) rock-buffered alteration zones.

Single-pass cooling model and metal solubility

Single-pass models were set up to simulate the pH,  $E_{\rm h}$ , total dissolved metal concentrations, and minerals precipitating from cooling the model input fluids from 350° to 100°C. At each step, 1 kg of fluid is moved along a fluid conduit with 25 nodes cooled by 5°C each, where any precipitated mineral is left behind in the previous node. This model assumes no interaction with the wall rocks and essentially simulates the solubility of metals within the stockwork zone of the sulfide occurrences or within individual black smokers (Fig. 1). The emphasis of these models is placed on the relative mobility of different metals rather than absolute values because the metal concentrations in the model input fluids were obtained from equilibration with a sulfide assemblage and are not those occurring in natural vent fluids.

The Vienna Woods fluid is reduced with a high pH value and low calculated metal solubility (Fig. 8; Table 6). The low initial metal concentrations of the Vienna Woods model input fluid led to the precipitation of comparably small amounts of minerals, notably no chalcopyrite forms at high temperature. Solubility contours (Fig. 8c) are steep for Fe and Te, which form a high-temperature zone comprising pyrite, calaverite, and hessite between 350°and 300°C (Fig. 8d). Solubility contours for Au, Ag, Cu, and Zn are relatively flat at elevated temperature (Fig. 8c) and then sharply decrease below 200°C, forming a zone comprising electrum, covellite, and sphalerite (Fig. 8d). Finally, galena precipitates as the last mineral at temperatures below 120°C.

The Fenway fluid reaches pH values <2 when cooled to  $100^{\circ}$ C, with a corresponding increase in  $E_h$  values to almost

<sup>&</sup>lt;sup>1</sup> Saturated minerals at the given pressure and temperature

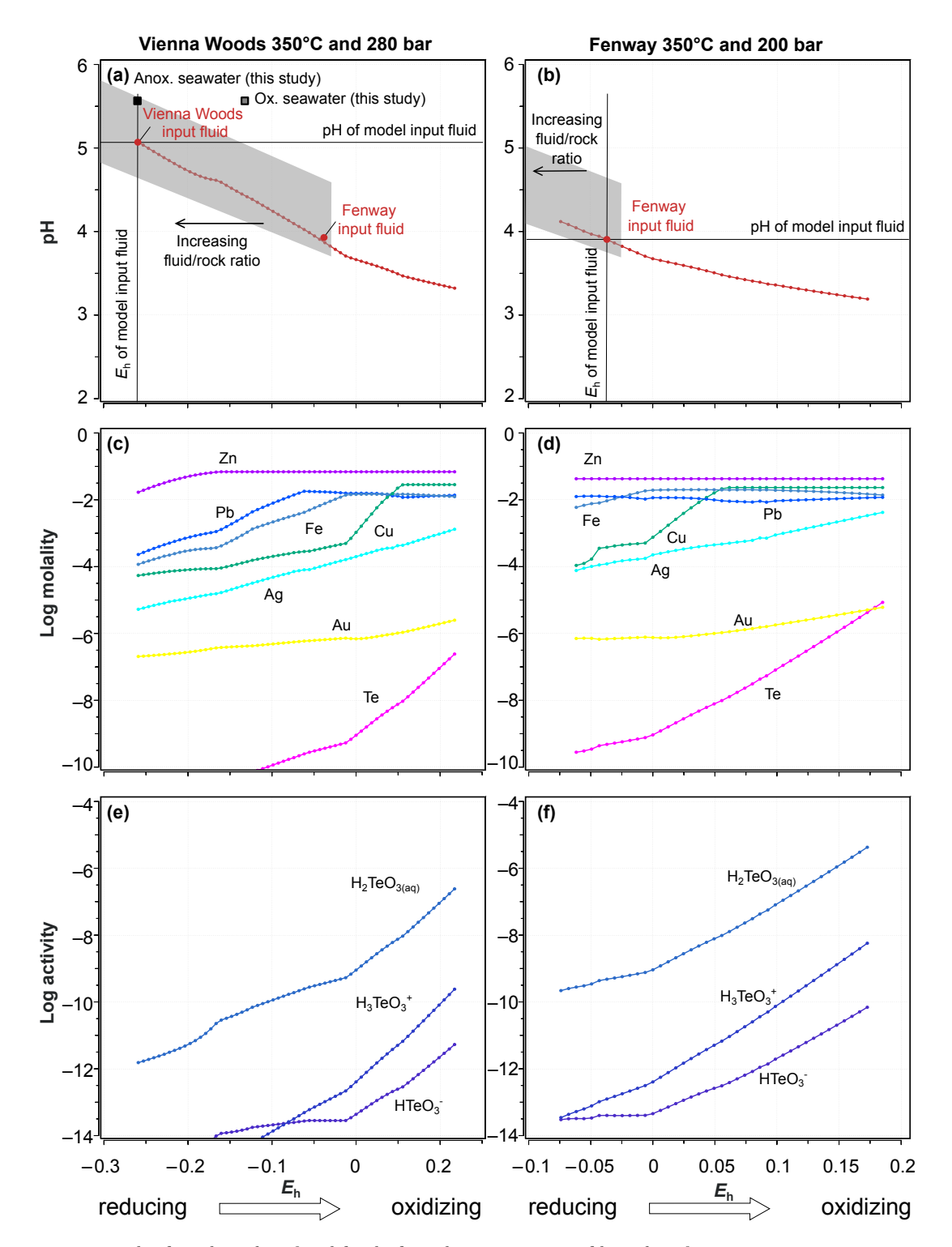


Fig. 6. Simulated pH, logarithm of total dissolved metal concentrations, and logarithm of aqueous Te species activities as a function of redox potential ( $E_h$  in V) for (a, c, e) Vienna Woods vent fluid at 350°C and 280 bar, and (b, d, f) Fenway vent fluid at 350°C and 200 bar. The input model compositions are listed in Table 6. Gray shaded areas indicate pH- $E_h$  values for rock-equilibrated vent fluids from Pierre at al. (2018). The gray square is oxidized seawater, and the black square is anoxic seawater given in Table 5.

 $0.2~\mathrm{V}$  (Fig. 9). At these conditions, Fe, Pb, and Zn remain soluble, whereas considerable Ag, Au, Cu, and Te precipitation occurs upon cooling, which is reflected in decreasing molality of dissolved metals in the fluid (Fig. 9c). Although Te concentration

trations in the model fluid are relatively low, the more oxidized starting conditions of this fluid permit transport of Te between ~250° and 350°C. The minerals precipitated from the Fenway model fluid include chalcopyrite and calaverite at 350°C,

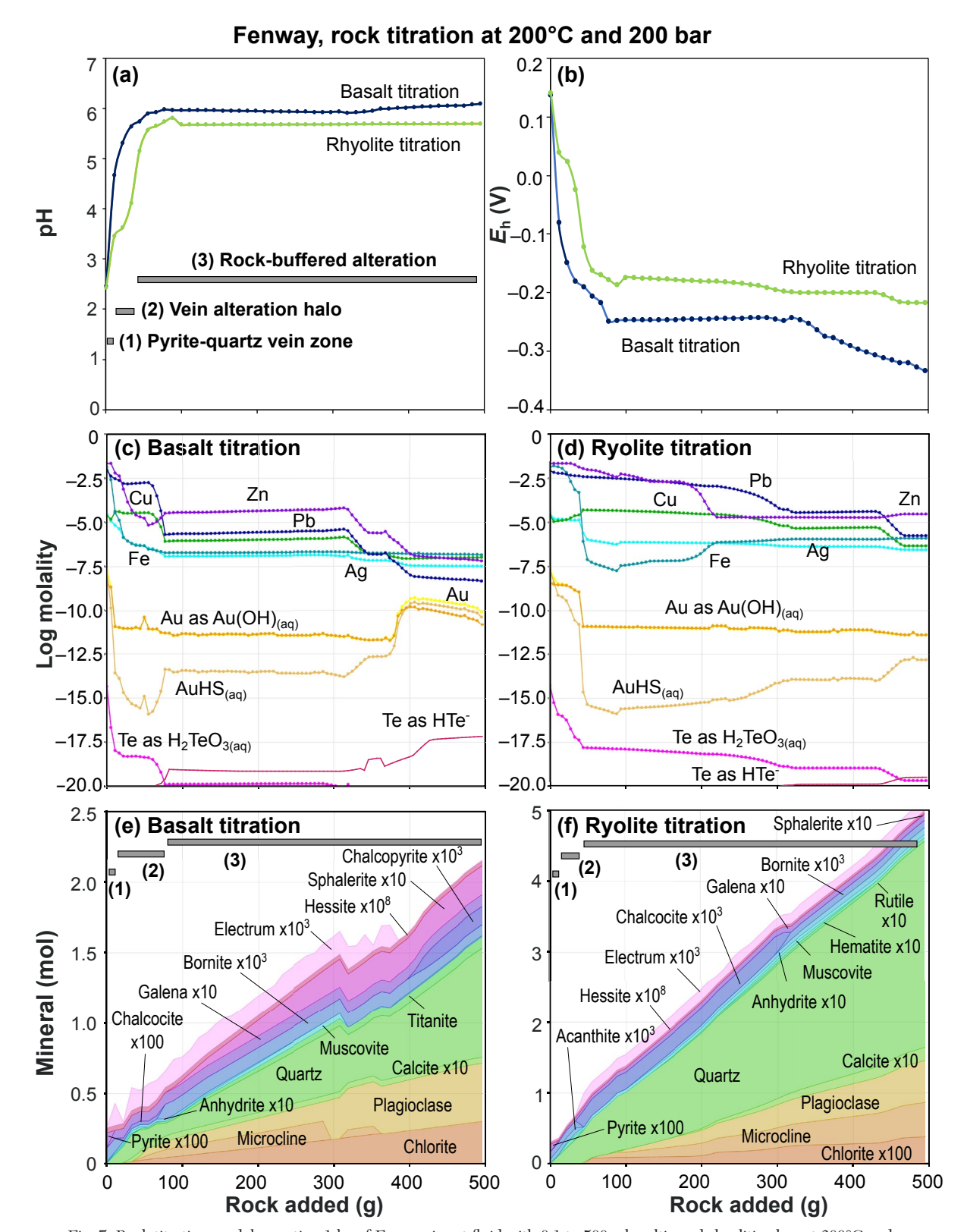


Fig. 7. Rock titration models reacting 1 kg of Fenway input fluid with 0.1 to 500 g basaltic and rhyolitic glass at 200°C and 200 bar. Changes in (a) pH and (b)  $E_h$  as a function of fluid-rock reaction showing generally three distinct zones. c, d) Total dissolved metals generally decrease with increasing fluid-rock reaction except for Au solubility, which increases due to the increased stability of AuHS $_{(aq)}$  and, to a lesser extent, Te due to increased stability of HTe $^-$ . e, f) Alteration (chlorite, microcline, plagioclase, quartz, pyrite, anhydrite, muscovite, calcite, rutile, and titanite) and ore minerals are similar but show different proportions and zones for the two rocks. The composition of basaltic glass is taken from Gysi and Stefansson (2011) and that of rhyolitic glass is taken from Bailey et al. (1989).

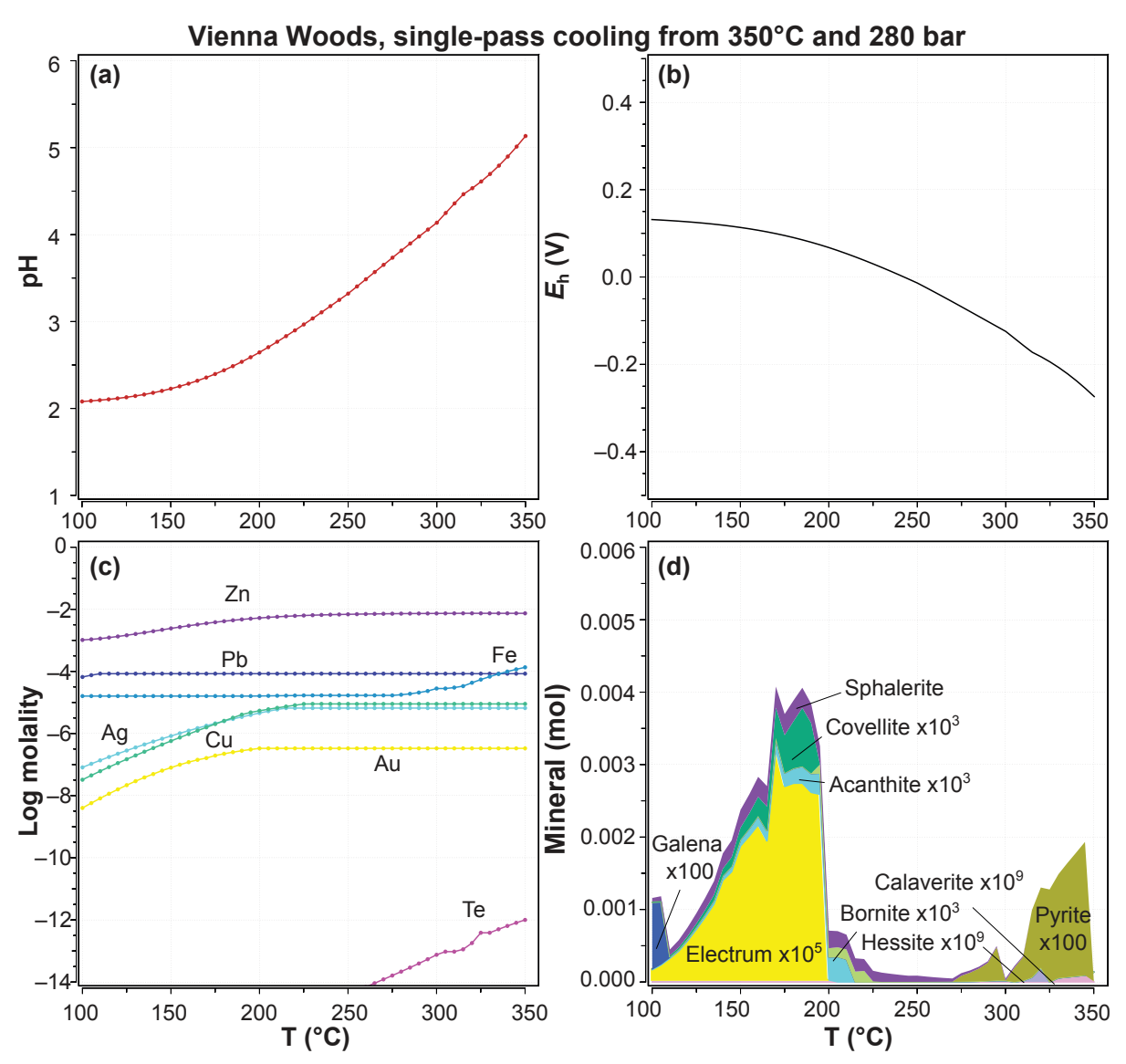


Fig. 8. Simulated single-pass cooling model of Vienna Woods vent fluid from 350° to 100°C at 200 bar showing (a) pH, (b)  $E_{\rm h}$ , (c) logarithm of total dissolved metal concentrations, and (d) mol minerals precipitated upon cooling. The input model composition of the Vienna Woods fluid is listed in Table 6. Multipliers were added to better illustrate mol of minerals precipitated and resulting zoning.

followed by electrum, pyrite, and hessite between 275° and 325°C, and bornite and acanthite below 250°C (Fig. 9d).

# Open-system transport, cooling, and seawater mixing models

The cooling behavior of the Vienna Woods and Fenway model input fluids was further investigated in two different open-system models (Fig. 10). Simplified transport models were conducted using the GEM2MT module, which allows for automation of one-dimensional (1-D) reactive mass transport simulations coupled with GEM calculation of equilibrium states in spatially distributed nodes over time steps. The approach was to simulate mineral precipitation and dissolution in a fluid conduit segmented into 50 nodes with temperatures decreasing from 350° to 100°C at 5°C increments. The first model investigates a sequential reactor chain with "waves" of

fluid passing through all nodes with a total of 1,000 waves of fluid (Fig. 10a, c). The second model is a simplified reactive mass transport model, which couples fluid flushing and geochemical reactions in each node at each step. This model consists of a series of flow-through reactors with a constant flux of input vent fluid in the first node (and output in the last node) and a simultaneous constant flux between each of the subsequent nodes that contain initially heated seawater (Fig. 10b, d). This model is analogous to a 1-D advective transport model, with time being reduced to steps where constant fluxes and mixing between nodes are considered for 1,000 steps, but for simplicity, no other hydrological parameters were included.

The resulting sequential waves model and the 1-D reactive transport model demonstrate that cooling of the Vienna Woods model fluid results in no significant precipitation of Te due to its low solubility in the starting fluid (Table 6). The

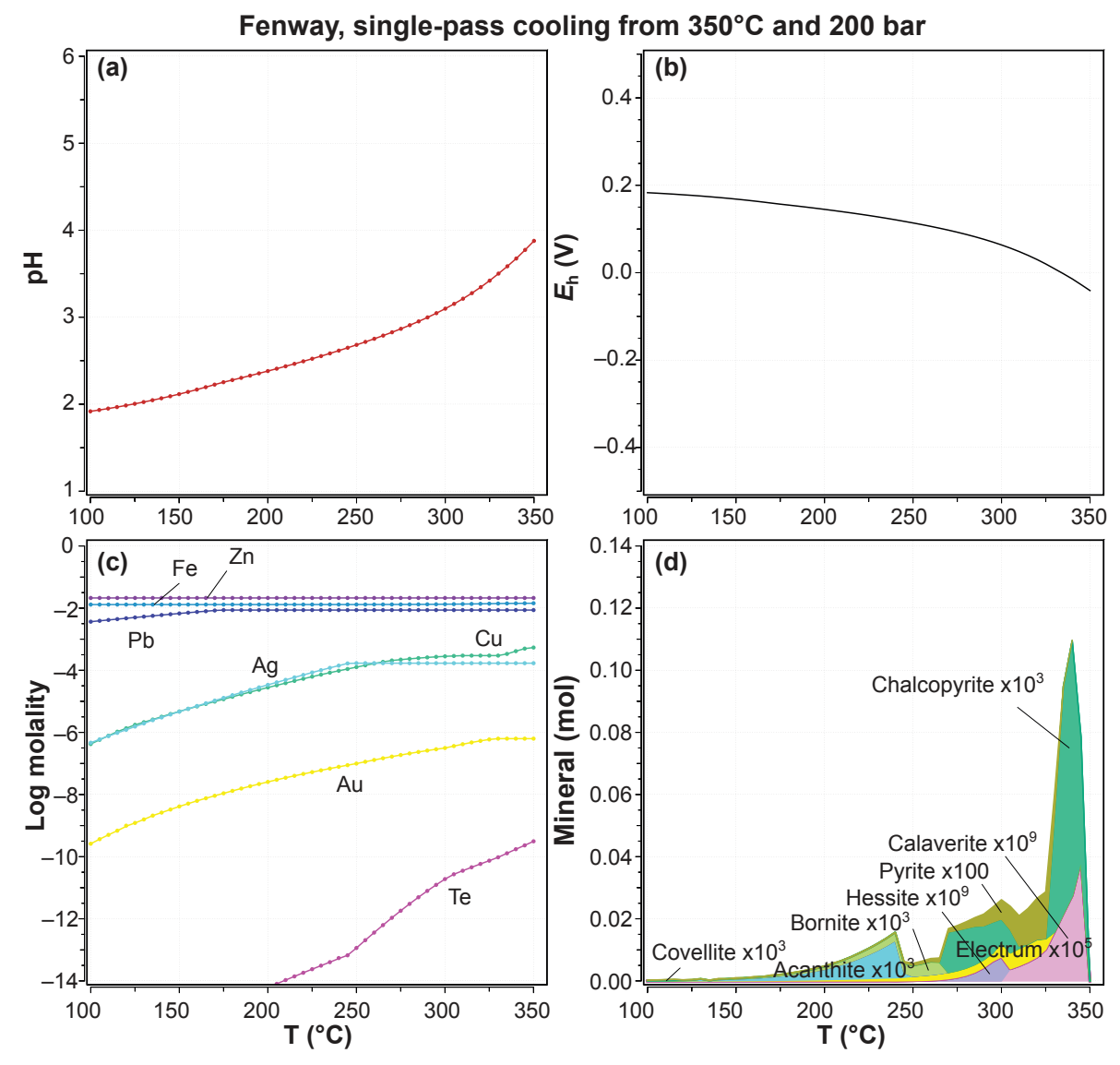


Fig. 9. Simulated single-pass cooling model of Fenway vent fluid from  $350^{\circ}$  to  $100^{\circ}$ C at 200 bar showing (a) pH, (b)  $E_h$ , (c) logarithm of total dissolved metal concentrations, and (d) mol minerals precipitated upon cooling. The input model composition of the Fenway fluid is listed in Table 2. Multipliers were added to better illustrate mol of minerals precipitated and resulting zoning.

model for Vienna Woods resulted in the notable development of a high-temperature  $(250^{\circ}\text{--}350^{\circ}\text{C})$  pyrite zone containing minor calaverite and hessite (Fig. 10a, b). A zone enriched in Zn-Cu-Ag-Au developed at intermediate temperatures  $(100^{\circ}\text{--}250^{\circ}\text{C}).$  In this zone, Zn occurs in sphalerite, Cu in bornite and covellite, Ag in a canthite, and Au as Au-rich electrum. The Vienna Woods model predicts galena precipitation at even lower temperatures of  $<150^{\circ}\text{C}.$  Galena occurs together with a canthite, covellite, and sphalerite.

Comparison of the sequential waves model and the 1-D reactive transport model indicates that cooling of the Fenway model fluid from 350° down to 250°C results in the development of a Cu-Te-(Au)–rich zone (Fig. 10c). In the sequential reactor model, high amounts of Ag, Au, Cu, and Te were precipitated and form a high-temperature chalcopyrite-hessite-electrum-pyrite zone and an intermediate-tempera-

ture bornite-acanthite zone (Fig. 10c). Mixing with seawater led to the precipitation of abundant anhydrite and minor pyrite as well as chalcopyrite and hessite at high temperature after 1,000 steps (Fig. 10d). Electrum precipitated and redissolved along the mixing front between vent fluid and seawater and completely disappeared after 500 steps. In general, the amount of metal precipitated at Fenway is one to two orders of magnitude higher than in the case of the mafic-hosted Vienna Woods model.

# Discussion

Tellurium and metal concentrations in hydrothermal vent fluids

The numerical simulations of this study provide important insights into metal mobility and deposition in sea-floor hydro-

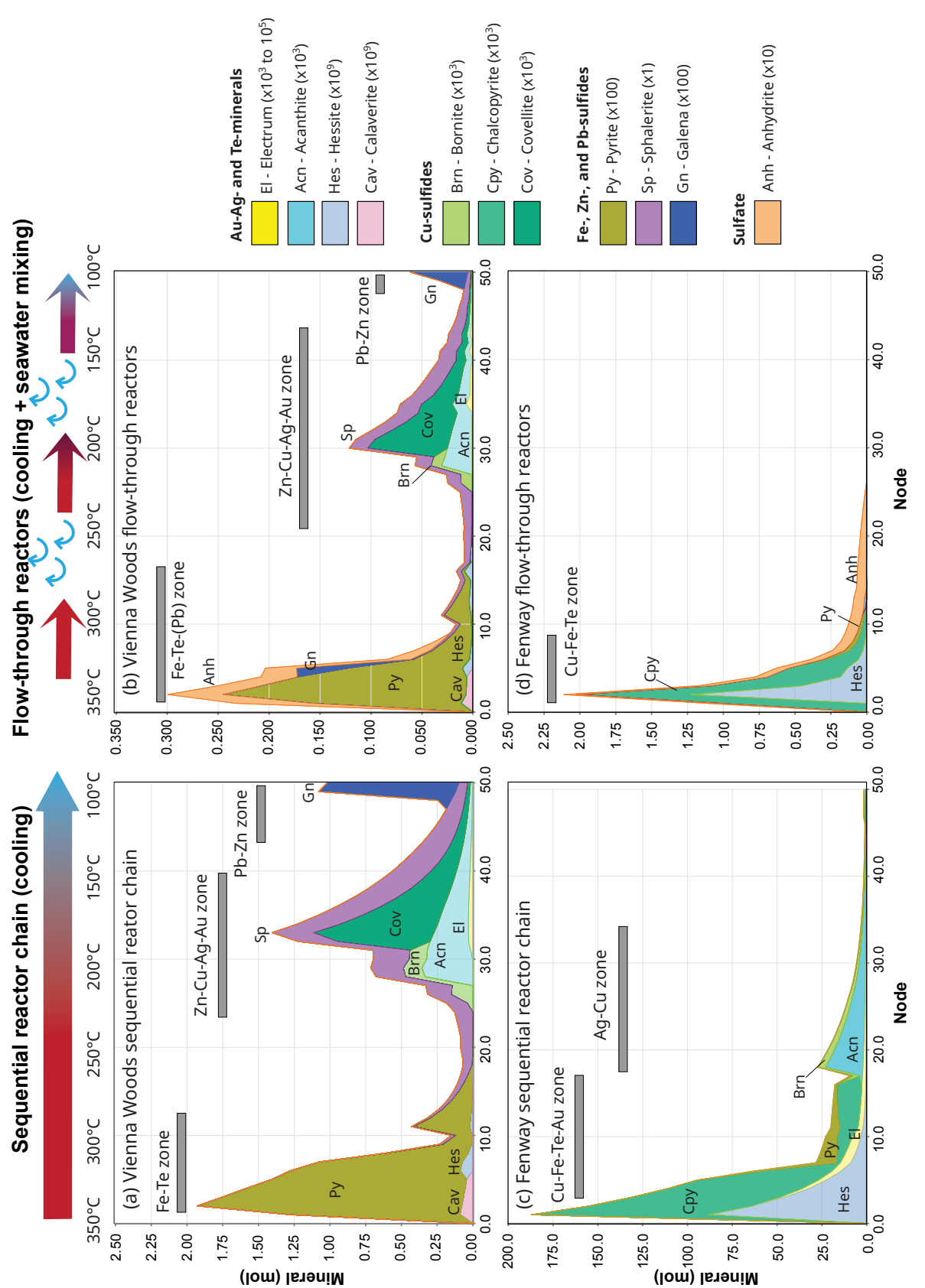


Fig. 10. Simulated 1-D reactive transport models showing sequential reactor chain cooling and flow-through reactors with cooling and seawater mixing models. a, b) Simulated mineralogy of cooled Vienna Woods vent fluid showing the development of a high-temperature Fe-Te-rich zone >300°C and a Zn-Cu-Ag-Au-rich zone at low temperature between 100° and 250°C. c, d) Simulated mineralogy of cooled Fenway vent fluid showing the development of a Cu-Fe-Te-(Au)-rich zone between 250° and 350°C and a low-temperature Ag ± Cu zone. Multipliers were added to improve illustration of mineral zoning.

thermal systems, including mineral paragenesis and metal zoning. However, it is difficult to quantitatively establish absolute metal concentrations for the hydrothermal fluids, as a series of assumptions needs to be made. In this contribution, the major model assumption is that the metal concentrations of the model vent fluids can be derived from the metal solubility of native metals and sulfide minerals at 350°C. The approach chosen provided an estimate for the upper concentration limits in hydrothermal vent fluids, permitting the study of relative metal mobility. Comparison between the compositions derived for the model vent fluids (Table 6) and direct measurements of hydrothermal vent fluids (Table 7) provide important insights into the applicability of the modeling approach.

At present, the Te content of sea-floor hydrothermal vent fluids has not been established through direct measurement. However, some Te measurements are available for the deep liquids of the Reykjanes geothermal system in Iceland, which has a geologic and tectonic setting that is analogous to that of black smoker hydrothermal systems hosted by mafic rocks. Hardardóttir et al. (2009) showed that the seawater-dominated hydrothermal fluids contain 19 to 60 ppb Te. Deep liquids in other geothermal systems typically contain between <0.1 and 4.5 ppb Te, with the highest value recorded being 2.94 ppm (Simmons and Brown, 2006; Simmons et al., 2016). The Te concentrations of geothermal liquids are orders of magnitude higher than the modeled Te content of 0.2 ppt calculated for the mafic-hosted Vienna Woods site and 50 ppt in the model fluid of the felsic-hosted Fenway site (Table 6).

Comparison between the model hydrothermal fluids and measured geothermal liquids reveals that Te concentrations are comparably low in the modeled fluids. At neutral pH and reducing conditions, Te enters a minimum solubility field (Fig. 5b), where the dominant species switches from  $H_2 TeO_{3(aq)}$  to  $H Te^-$ . These conditions are comparable to basalt-buffered sea-floor hydrothermal fluids (Fig. 7a, b; Pierre et al., 2018), in which Te mobility is limited. Stability fields and predicted Te solubility at elevated temperature are also consistent with simulations presented in Grundler et al. (2013), except that the HTe<sup>-</sup> field extends to higher pH in this study because the ditelluride species was not included. Simmons et al. (2016) suggested that the ditelluride species dominates in the deep geothermal fluids from the Taupo volcanic zone, which have alkaline pH values of 6 to 7 and are highly reduced. Their modeled Te concentrations, however, still underestimate measured concentrations at those conditions by up to ~1 order of magnitude, indicating supersaturation with respect to telluride minerals (Simmons et al., 2016). The underestimation of Te concentrations in model fluids suggests that future revisions of the underlying thermodynamic data may be needed, especially for the ditelluride species at highly reducing conditions.

There are currently only a few studies that have recorded the concentrations of precious metals in hydrothermal vent fluids (Fuchs et al., 2019). These suggest that Ag concentrations range from 0.3 to 43 ppb, while the Au content varies from 0.02 to 0.94 ppb (Table 7). Liquids sampled from deep geothermal wells contain up to 2.4 ppm Ag and 23 ppb Au (Simmons and Brown, 2006; Hardardóttir et al., 2009; Hannington et al., 2016; Simmons et al., 2016). In comparison, the Vienna Woods model fluid has 0.5 ppm Ag and

37 ppb Au, while the Fenway model fluid contains 18 ppm Ag and 124 ppb Au (Table 6). Other measured metal concentrations in hydrothermal vent fluids include 0.001 to 26 ppm Cu, 0.2 to 1,340 ppm Fe, 0.3 to 1,450 ppb Pb, and 0.01 to 59 ppm Zn (Table 7). For comparison, the Vienna Woods model fluid contains 3 ppm Cu, 6 ppm Fe, 44 ppm Pb, and 1,013 ppm Zn. The Fenway model fluid is characterized by higher metal concentrations of 34 ppm Cu, 827 ppm Fe, 1,794 ppm Pb, and 1,393 ppm Zn (Table 6).

The agreement between the modeled concentrations of Cu and Fe in the model fluids with those observed in natural hydrothermal vent fluids provides confidence in the modeling results. However, the model fluids have Ag, Au, and Zn concentrations that are one order of magnitude higher than those in hydrothermal vent fluids. This may be related to the fact that the modeling was based on a maximum metal solubility at 350°C, which may be comparably high for hydrothermal vent fluids. Differences between the Pb content of the Vienna Woods and Fenway model fluids and the range of Pb concentrations in hydrothermal vent fluids (Table 6) may be related to the fact that the thermodynamic properties for Pb aqueous species have not been updated since the release of the Supcrt92 and slop98.dat data (Shock et al., 1997; Sverjensky et al., 1997), which are based on only limited experimental data obtained at temperatures below 300°C.

# Metal mobility in hydrothermal vent fluids

The simulations of this study provide important constraints on the factors affecting metal solubility in sea-floor hydrothermal systems, including temperature, pH,  $E_h$ , fluid mixing, and fluid-rock interaction. The predicted Te speciation as a function of pH and redox in seawater (Fig. 5) and the redox titrations (Fig. 6) indicate that Te solubility decreases in reduced fluids and has a minimum solubility at pH values of 6 and 7 at temperatures of 250° and 350°C, respectively. Simulated single-pass cooling models for the Vienna Woods and Fenway fluids (Figs. 8, 9) further indicate that metal solubility and pH decrease by cooling from 350° to 100°C, whereas  $E_h$  increases in the absence of fluid-rock reaction. At these conditions, Te solubility is controlled mainly by the  $H_2TeO_{3(aq)}$  species as well as the solubility of hessite and calaverite. The Te concentrations in the Vienna Woods and Fenway fluids decrease significantly with cooling, and Te becomes largely insoluble below 200°C (Figs. 8, 9).

The Ag, Au, and Cu (±Fe) concentrations in the Vienna Woods and Fenway fluids also decrease upon cooling but display different behaviors due to their different starting compositions. The Vienna Woods model input fluid has lower dissolved metal concentrations and shows a less pronounced decrease in Au, Cu, and Ag concentrations with decreasing temperatures when compared to the Fenway model. In the case of Vienna Woods, precipitation of Fe and Te occurs between 200° and 350°C, whereas Ag, Au, and Cu solubilities decrease drastically below 200°C. In addition to the stability of electrum and base metal sulfides, the formation of aqueous complexes is important in controlling the metal mobilities in the models. Silver, Cu, and Fe form stable chloride complexes that dominate at the simulated conditions, whereas Au can form hydroxyl, bisulfide, and chloride complexes that variably dominate speciation depending on temperature,

Table 7. Metal Content of Modern Sea-Floor Hydrothermal Vent Fluids and Deep Geothermal Liquids

	T		Cu	Fe	Zn	Pb	Ag	Au	Te	
Location	$^{\circ}\mathrm{C}$	рН	ppm	ppm	ppm	ppb	ppb	ppb	ppb	Ref
Edmond, CIR	273–382	3.0-3.1	7–26	586-1,335	8–10	166-261				1
Kairei, CIR	315-365	3.4 - 3.5	8-18	198-336	4-6	65-97				1
21°N, EPR	273-355	3.3-3.8	1–3	42-136	3–7	38 - 74	4			2
11–13°N, EPR	317–380	3.1 - 3.7	0.1 - 7	81-601		2-56				2
Brandon, EPR	368 – 405	3.1 - 5.1	3–7	372-698	5–8					3
EPR range	273-401	2.6 - 3.8	0.1 - 9	33-687	0.1-22	2-78	4	0.08		4, 5
Axial volcano, JFR	5-328	3.5 – 4.4	1	1–56	0.2 - 7	21-63				2
Cleft, JFR	262 - 327	2.8 – 3.1	0.1 - 0.6	77–916	10-39					6
South, JFR	224-340	3.2		578-1,047	59	187				2
Broken Spur, MAR	360		3	110	5					7
Logatchev, MAR	353	3.3	2	140	2	21	1			7
Lucky Strike, MAR	185–328	3.4 – 5.0	0.2 - 2	3-51	0.3 - 3	7-27	0.5 - 3			7, 8
Menez Gwen, MAR	271 - 284	4.4 – 4.5		1		4-12	2			7
Rainbow, MAR	362-365	2.7 - 3.2	7-10	1,340	7 - 12	27 - 35	5			7
Red Lion, MAR	349		0.3	45	4	87				9
Sisters Peak, MAR	400-464		7-22	189	24	83				9
Snakepit, MAR	341	3.7	2	134	4	62	3			7
TAG, MAR	363	3.1	8	289	5	23	6			7
Turtle Pits, MAR	405-407		0.6 - 7	174-220	2–5	12-39				9
MAR range	224-379	2.8 – 4.5	0.1-9	20-1,047	1-59	12 - 225				4
Guaymas basin	100-315	5.9	0.01 - 3	1–11	0.01 - 0.07	4-135	0.1 - 25			2
Okinawa trough	238	4.6 - 5.0	0.001	0.2	0.5	8				5
Pacmanus	268	2.6	17	134	40	1,450	43	0.94		4, 5
Vienna Woods	282	4.1	0.3	6	2	0.8	3	0.02		4, 5
Reykjanes geothermal liquid	284–296	$5.9^{1}$	1–17	45–136	20–26	124–290	0.3–104	1–6	19–60	10
Taupo geothermal liquid	166-320	5.2 - 7.2	$0.6-20^2$		$0.2 - 2.3^2$	$0.3 - 808^2$	$1-2,400^2$	$0.1 - 23^2$	$1-2,940^2$	11
Range in natural fluids	5-464	2.6–7.2	0.001-26	0.2–1,340	0.01 – 59	0.3–1,450	0.1 - 2,400	0.02 – 23	1-2,940	

References: 1 = Gallant and Von Damm (2006), 2 = Von Damm (1990), 3 = Von Damm et al. (2003), 4 = Hannington et al. (2005), 5 = Fuchs et al. (2019), 6 = Butterfield and Massoth (1994), 7 = Douville et al. (2002), 8 = Von Damm et al. (1998), 9 = Koschinsky et al. (2008), 10 = Hardardóttir et al. (2009), 11 = Simmons et al. (2016)

Abbreviations: CIR = Central Indian Ridge, EPR = East Pacific Rise, JFR = Juan de Fuca Ridge, MAR = Mid-Atlantic Ridge

<sup>1</sup>pH measured on surface

pH, and redox. Lead and Zn form chloride complexes and remain largely mobile in the simulated fluids because of the decrease in pH during cooling and availability of Cl- for complexation with these metals. In the case of the Vienna Woods model, sphalerite precipitation occurs in the single-pass cooling model (Fig. 8). In contrast, sphalerite precipitation is only observed in the rock titration models for Fenway due to a decrease in redox state (Fig. 7). The solubility of other metals decreases considerably with increasing fluid-rock reaction (Fig. 7c, d). However, Au in the form of bisulfide complexes and Te as HTe<sup>-</sup> may show increased solubility with increasing fluid-rock reaction in basalt-equilibrated simulations at reducing conditions (Fig. 7c). Finally, the more complex reactive transport models (Fig. 10) indicate that fluid mixing of simulated vent fluids with entrained seawater and simultaneous cooling result in increased oxidation of the fluids, overall enhancing metal solubility in any given temperature interval. Nevertheless, the speciation, mineralogy, and metal zoning obtained in fluid mixing models are similar to those of the cooling models, as can be seen by comparing Figures 8 and 9 with Figure 10.

The chemistry of the Vienna Woods vent fluids can be best explained as a result of the interaction and buffering of heated seawater with basaltic rocks (Pierre et al., 2018). Therefore, Vienna Woods is a good example of a rock-buffered sea-floor system located on a back-arc spreading center. The comparably high fluid pH and the more reduced  $E_h$  values both limit the solubility of ore minerals in the vent fluids (Fig. 8). This contrasts with the situation at Fenway, which is located in a felsicdominated volcanic succession. The vent fluids at Fenway have an overall lower pH and higher redox state and, therefore, have a higher capacity to dissolve metals including Te at temperatures between 250° and 350°C (Fig. 9). However, fluid-rock interaction of the Fenway fluids as simulated by the rock titration models can result in a sharp decrease in metal solubilities with increased rock buffering and increased fluid reduction. Based on these observations, it is concluded that Te transport and enrichment in sea-floor hydrothermal fluids are optimized if fluid-rock interaction is minimal, requiring vents to be located above well-established, high-flux fluid upflow zones (Fig. 1). At these flow conditions, the hydrothermal fluids reach temperatures >250°C, remain oxidized, and keep

<sup>&</sup>lt;sup>2</sup>Elevated field blanks of up to 0.23 ppm Zn, 9.4 ppm Cu, 52 ppb Pb, 31 ppb Ag, 11 ppb Te, and 2 ppb Au

their low initial pH values, allowing for high dissolved metal concentrations and efficient metal precipitation as a function of cooling. Changes in flux could result in variability of fluid to rock ratios (i.e., fluid-rock reaction paths), which in turn could modulate metal contents in vent fluids over time.

#### Comparison to modern sea-floor hydrothermal systems

Natural sea-floor massive sulfides show distinct zones of pyrite-chalcopyrite ± gold, chalcopyrite-(bornite-covellite)sphalerite ± gold ± acanthite, and sphalerite-galena-acanthite ± sulfosalts (Fig. 1), resulting in distinct enrichment in Cu-Fe  $\pm$  Au, Zn-Cu  $\pm$  Ag  $\pm$  Au, and Zn-Pb-Ag, respectively. These zones correspond to metal zoning in the 1-D reactive mass transport simulations, which are largely temperaturecontrolled, comprising high-temperature Cu-Fe-Te ± Au, intermediate-temperature Zn-Ag  $\pm$  Cu  $\pm$  Au, and low-temperature Pb-Zn  $\pm$  Ag zones (Fig. 10). Coexistence of ore minerals in a zone can be considered a positive correlation of ore metals, whereas ore minerals occurring in different zones would constitute a negative metal correlation between the zones and their metals, respectively. This provides a simple concept for comparing metal zoning in 1-D reactive mass transport simulations to metal ratios in natural massive sulfides hosted by mafic and felsic host-rock successions.

The results of the simulations using the Vienna Woods model fluid can be compared to basalt-hosted sea-floor hydrothermal vents located in mature back-arc basins or those associated with mid-ocean ridges. In the Vienna Woods simulations, a high-temperature Fe-Te zone is developed that contains pyrite as well as minor calaverite and hessite (Fig. 10a, b). In pyrite-rich samples from the modern sea floor, elevated Te contents of up to 20 ppm have been encountered (Monecke et al., 2016). The 1-D reactive mass transport simulations for Vienna Woods yield an intermediate-temperature  $Zn-Ag \pm Cu \pm Au$  zone, which consists of abundant sphalerite and minor acanthite, covellite, bornite, and electrum. In addition, a low-temperature Pb-Zn ± Ag zone containing galena and sphalerite with minor acanthite was simulated. The modeling results agree well with element correlations observed in sea-floor sulfides from typical basalt-hosted hydrothermal vent systems, most notably the negative correlations between Zn, Pb, and Au with the Cu/Ag ratio (Fig. 3c-e).

The simulations using the Fenway model fluid are in broad agreement with the limited data available for hydrothermal systems located in felsic-dominated rifted arcs. The predicted association between Te minerals and Cu and Fe sulfides is apparent in element correlation diagrams, where a positive correlation can be observed between Te and Fe with the Cu/Ag ratio (Fig. 3a, b). There is a negative correlation between Zn and Pb with the Cu/Ag ratio (Fig. 3c, d), and Au shows a weak positive correlation at low Cu/Ag ratios and a negative correlation at high Cu/Ag ratios (Fig. 3e). In the Fenway 1-D reactive mass transport simulations, the high-temperature Cu-Fe-Te  $\pm$ Au zone consists of chalcopyrite, electrum, hessite, and pyrite (Fig. 10c, d). This is consistent with the observed elemental correlations. The simulations of this study suggest the occurrence of hessite and calaverite. So far, however, only limited research has been conducted on the mineralogical occurrences of Te in hydrothermal sea-floor systems in this tectonic setting. Monecke et al. (2016) reported on the occurrence of tellurobismuthite in textural association with minerals of the tennantite-tetrahedrite solid solution at the PACMANUS vent field in the eastern Manus basin. In addition to tellurobismuthite, Maslennikov et al. (2017) reported the presence of hessite and native Te in assemblages with tennantite and bornite in chalcopyrite-rich chimneys. The occurrence of tellurobismuthite was not modeled in the present study because Bi was not considered in the simulations.

### Comparison to volcanogenic massive sulfide deposits

Sea-floor hydrothermal vent sites and associated sulfide deposits are close analogues to VMS deposits occurring in ancient volcanic terranes (Franklin et al., 2005; Hannington et al., 2005; Hannington, 2014). These deposits total an endowment of nearly 13.7 billion metric tonnes of polymetallic ores (Franklin et al., 2005), which contain Te concentrations of up to 100 ppm (Monecke et al., 2016). Based on the makeup of the volcanic host-rock succession, five lithostratigraphic types of VMS deposits are distinguished (Barrie and Hannington, 1999; Franklin et al., 2005). The results of the numerical modeling as well as the compilation of assay data of active sea-floor sulfide samples suggest that the composition of the volcanic host rocks is an important control on the Te content of VMS deposits.

As suggested by the numerical modeling and the active sea-floor sulfide data compilation, VMS deposits in host-rock successions dominated by mafic rocks appear to have low Te contents. This includes the Cretaceous massive sulfide deposits in Cyprus, which are hosted by pillow basalts of the Troodos ophiolite (Hannington et al., 1998). Pyrite and chalcopyrite are the main phases containing Te in the ores from these VMS deposits (Keith et al., 2016; Martin et al., 2018, 2020). Laser ablation-inductively coupled plasma-mass spectrometry (LA-ICP-MS) on pyrite yielded average Te concentrations of 6.0 to 17.3 ppm Te (Martin et al., 2018). No discrete Te minerals were identified (Keith et al., 2016; Martin et al., 2018, 2020).

This contrasts with VMS deposits in volcanic successions containing more abundant felsic rocks. The Kankberg deposit in the Skellefte district, Sweden, is hosted by bimodal-felsic volcanic rocks of the Paleoproterozoic Skellefte Group, which are interpreted to have formed in an island arc setting (Allen et al., 1996). Kankberg is currently the only VMS deposit that produces Te as a primary commodity (Åström, 2015), with its proven mineral reserve grading 194 g/t Te (Boliden, 2021). Gold-bearing tellurides in the ores of the Kankberg deposit, which have been overprinted at upper greenschist to amphibolite facies metamorphic conditions, include petzite, calaverite, and sylvanite. In addition, altaite, coloradoite, hessite, frohbergite, melonite, native tellurium, and tellurobismuthite are present (Åström, 2015).

Anomalous Te enrichment has also been recorded at the Bend VMS deposit, which forms part of the Paleoproterozoic Penokean greenstone belt stretching from Wisconsin into Michigan, USA. The deposit is hosted in a bimodal-mafic succession (Franklin et al., 2005). Twelve representative massive sulfide samples collected from Bend yielded an average Te concentration of 635 g/t (Woodruff et al., 2003). The massive sulfides, which have been overprinted at greenschist metamorphic conditions, contain altaite, calaverite, frohbergite,

krennerite, petzite, sylvanite, and native tellurium as accessory phases (DeMatties and Rowell, 1996; Quigley, 2016).

The Ordovician Ming deposit in Newfoundland, Canada, is hosted in a bimodal-mafic volcanic succession (Franklin et al., 2005). Massive sulfides in the different ore zones average 10 to 90 ppm Te. Altaite, hessite, and tsumoite are the most abundant Te minerals (Brueckner et al., 2016). The Devonian Yubileynoe VMS deposit in the southern Urals of Russia (Tseluyko et al., 2019) is also hosted by a bimodal-mafic volcanic succession. Tellurium averages 20.4 ppm in the Cu-rich massive sulfides of this deposit. Pyrite contains Te concentrations ranging up to ~2,700 ppm in black smoker chimney fragments (Tseluyko et al., 2019). The massive sulfide ores, which have been overprinted at prehnite-pumpellyite metamorphic grades, contain abundant Te-bearing minerals, including altaite, calaverite, coloradoite, hessite, petzite, rucklidgeite, stützite, tellurobismuthite, and volynskite (Tseluyko et al., 2019).

Although comparison with the characteristics of VMS deposits appears to support the main findings of the modeling of this study, the mineralogical sequestration of Te in VMS deposits appears to be more complicated than predicted by the modeling or observed in modern sea-floor sulfides. Monecke et al. (2016) suggested that the formation of Te minerals is related to the metamorphic recrystallization or remobilization of the massive sulfides at greenschist facies and higher metamorphic grades. During recrystallization, Te originally contained in the crystal structure of the major ore minerals is expelled from these phases and forms new accessory Te minerals that are located along the margins of the recrystallized sulfide grains, at triple junction contacts, or in late remobilization veins.

#### Conclusions

This study provides the first comprehensive review of the behavior of Te in sea-floor hydrothermal systems, constraining the mobility and deposition of this important trace element. The simulations conducted in this study show that fluid redox and temperature represent first-order controls on enrichment of Te in massive sea-floor sulfides.

The simulation results of this study were compared to observations made in natural systems. Identified host-rock controls and predicted metal associations were tested against a large data set of geochemical analyses of sulfide samples from seafloor hydrothermal vent sites. Metal concentrations modeled for hydrothermal fluids were validated against the concentration ranges of these metals encountered in sea-floor hydrothermal vent fluids and deep geothermal liquids. In addition, available literature on massive sulfide deposits hosted in ancient volcanic successions was reviewed. These comparisons confirm that the redox and temperature of hydrothermal fluids indeed are the most important controls on Te mobility and deposition in modern and ancient sea-floor hydrothermal systems. Sulfides from felsic-hosted vents show systematic correlations between the Te concentrations and the abundances of precious and base metals. Tellurium enrichment occurs in high-temperature Cu- and Fe-bearing minerals. Comparison of the modeling results and the bulk chemical analyses of seafloor sulfides indicates that the Cu/Ag ratio is a useful proxy for the temperature of sulfide formation and can also be used as a proxy for Te enrichment.

The simulations with available thermodynamic data indicate that Te is transported as a Te(IV) hydroxyl species and becomes largely immobile at rock-buffered reducing conditions in felsic- and mafic-hosted hydrothermal systems investigated in this study. However, this review shows important limitations that need to be overcome in the future. Aqueous Te(IV) species compare well between thermodynamic predictions and experimental data up to 200°C, presented in the experimental study by Grundler et al. (2013). However, prediction of the stability of the reduced Te(-II) and polytelluride (Te<sub>2</sub><sup>2</sup>) species relies on thermodynamic extrapolations of low-temperature experimental data and has not been verified experimentally at hydrothermal conditions. These reducing Te species are relevant to predicting Te mobility at highly reducing conditions, such as, for example, ultramafic-hosted hydrothermal systems. Calaverite, hessite, and native tellurium are the only stable Te minerals that were in equilibrium with hydrothermal fluids in the simulations of this study. Despite these minerals being well known to occur in active sea-floor massive sulfides, other Tebearing minerals with additional elements may need to be considered in future modeling studies, such as coloradoite (HgTe), melonite (NiTe<sub>2</sub>), tellurobismuthite (Bi<sub>2</sub>Te<sub>3</sub>), and tetradymite (Bi<sub>2</sub>Te<sub>2</sub>S), as well as the occurrences of Te as a trace element in Cu-Fe sulfides. The importance of Te as a critical element, therefore, calls for experimental and calorimetric data to better determine the thermodynamic properties for Te-bearing minerals and aqueous species at hydrothermal conditions.

# Acknowledgments

We thank Dmitrii Kulik for explanation and development of help files for the GEM2MT reactive transport module in the GEM-Selektor code package. We are grateful for constructive comments by reviewers J. Majzlan and B. Tutolo, as well as handling of the manuscript by associate editor G. Pokrovski.

#### REFERENCES

Akinfiev, N.N., and Tagirov, B.R., 2014, Zn in hydrothermal systems: Thermodynamic description of hydroxide, chloride, and hydrosulfide complexes: Geochemistry International, v. 52, p. 197–214.

Akinfiev, N.N., and Zotov, A.V., 2001, Thermodynamic description of chloride, hydrosulfide, and hydroxo complexes of Ag(I), Cu(I), and Au(I) at temperatures of 25–500°C and pressures of 1–2000 bar: Geochemistry International, v. 39, p. 990–1006.

——2010, Thermodynamic description of aqueous species in the system Cu–Ag–Au–S–O–H at temperatures of 0–600°C and pressures of 1–3000 bar: Geochemistry International, v. 48, p. 714–720.

Allen, R.L., Weihed, P., and Svenson, S.Å., 1996, Setting of Zn-Cu-Au-Ag massive sulfide deposits in the evolution and facies architecture of a 1.9 Ga marine volcanic arc, Skellefte district, Sweden: Economic Geology, v. 91, p. 1022–1053.

Åström, O., 2015, Evaluation and modeling of trace elements from drillcore analysis at Kankberg Au-Te mine, Skellefte district, Sweden: M.Sc. thesis, Luleå, Sweden, Luleå University of Technology, 28 p.

Bailey, R.A., Miller, C.D., and Sieh, K., 1989, Long Valley Caldera and Mono Inyo Craters volcanic chain, eastern California, *in* Chapin, C.E., and Zidek, J., eds., Field excursions to volcanic terranes in the western United States, IAVCEI General Assembly, Santa Fe, New Mexico, June 25 – July 1, 1989, Volume 2 Cascades and intermountain West: Socorro, New Mexico Bureau of Mines and Mineral Resources, p. 227–254.

Barin, I., 1995, Thermochemical data of pure substances, 3rd ed.: Weinheim, VCH Verlagsgesellschaft, 1885 p.

Barrie, C.T., and Hannington, M.D., 1999, Classification of volcanic-associated massive sulfide deposits based on host-rock composition: Reviews in Economic Geology, v. 8, p. 1–11.

- Berkenbosch, H.A., de Ronde, C.E.J., Gemmell, J.B., McNeill, A.W., and Goemann, K., 2012, Mineralogy and formation of black smoker chimneys from Brothers submarine volcano, Kermadec Arc: Economic Geology, v. 107, p. 1613–1633.
- Bindi, L., Carbone, C., Belmonte, D., Cabella, R., and Bracco, R., 2013, Weissite from Gambatesa mine, Val Graveglia, Liguria, Italy: Occurrence, composition and determination of the crystal structure: Mineralogical Magazine, v. 77, p. 475–483.
- Boliden, 2021, Annual and sustainability report 2021: Boliden, https://reports.boliden.com/globalassets/2021/pdf/boliden\_asr2021\_eng.pdf.
- Brueckner, S.M., Piercey, S.J., Pilote, J.L., Layne, G.D., and Sylvester, P.J., 2016, Mineralogy and mineral chemistry of the metamorphosed and precious metal-bearing Ming deposit, Canada: Ore Geology Reviews, v. 72, p. 914–939.
- Brugger, J., Etschmann, B., Liu, W., Testemale, D., Hazemann, J.L., Emerich, H., van Beek, W., and Proux, O., 2007, An XAS study of the structure and thermodynamics of Cu(I) chloride complexes in brines up to high temperature (400°C, 600 bar): Geochimica et Cosmochimica Acta, v. 71, p. 4920–4941.
- Brugger, J., Etschmann, B.E., Grundler, P.V., Liu, W., Testemale, D., and Pring, A., 2012, XAS evidence for the stability of polytellurides in hydrothermal fluids up to 599°C, 800 bar: American Mineralogist, v. 97, p. 1519–1522.
- Butterfield, D.A., and Massoth, G.J., 1994, Geochemistry of north Cleft segment vent fluids: Temporal changes in chlorinity and their possible relation to recent volcanism: Journal of Geophysical Research, v. 99, p. 4951–4968.
- DeMatties, T.A., and Rowell, W.F., 1996, The Bend deposit: An early Proterozoic copper-gold VMS deposit [ext. abs.]: Annual Institute on Lake Superior Geology, 42nd, Cable, Wisconsin, 1996, Proceedings, p. 143–159.
- Douville, E., Charlou, J.L., Oelkers, E.H., Bienvenu, P., Jove Colon, C.F., Donval, J.P., Fouquet, Y., Prieur, D., and Appriou, P., 2002, The Rainbow vent fluids (36°14'N, MAR): The influence of ultramafic rocks and phase separation on trace metal content in Mid-Atlantic Ridge hydrothermal fluids: Chemical Geology, v. 184, p. 37–48.
- Driesner, T., and Heinrich, C.A., 2007, The system  $\rm H_2O-NaCl.$  Part I: Correlation formulae for phase relations in temperature–pressure–composition space from 0 to 1000°C, 0 to 5000 bar, and 0 to 1  $X_{\rm NaCl}$ : Geochimica et Cosmochimica Acta, v. 71, p. 4880–4901.
- Echmaeva, E.A., and Osadchii, E.G., 2009, Determination of the thermodynamic properties of compounds in the Ag-Au-Se and Ag-Au-Te systems by the EMF method: Geology of Ore Deposits, v. 51, p. 247–258.
- Etschmann, B.E., Liu, W., Pring, A., Grundler, P.V., Tooth, B., Borg, S., Testemale, D., Brewe, D., and Brugger, J., 2016, The role of Te(IV) and Bi(III) chloride complexes in hydrothermal mass transfer: An X-ray absorption spectroscopic study: Chemical Geology, v. 425, p. 37–51.
- Filella, M., and May, P.M., 2019, The aqueous chemistry of tellurium: Critically-selected equilibrium constants for the low-molecular-weight inorganic species: Environmental Chemistry, v. 16, p. 289–295.
- Firstova, A., Stepanova, T., Sukhanova, A., Čherkashov, G., and Poroshina, I., 2019, Au and Te minerals in seafloor massive sulphides from Semyenov-2 hydrothermal field, Mid-Atlantic Ridge: Minerals, v. 9, article 294.
- Fortier, S.M., Nassar, N.T., Graham, G.E., Hammarstrom, J.M., Day, W.C., Mauk, J.L., and Seal, R.R., 2022, USGS critical minerals review: Mining Engineering, v. 74, p. 34–48.
- Fouquet, Y., Cambon, P., Etoubleau, J., Charlou, J.L., Ondréas, H., Barriga, F.J.A.S., Cherkashov, G., Semkova, T., Poroshina, I., Bohn, M., Donval, J.P., Henry, K., Murphy, P., and Rouxel, O., 2010, Geodiversity of hydrothermal processes along the Mid-Atlantic Ridge and ultramafic-hosted mineralization: A new type of oceanic Cu-Zn-Co-Au volcanogenic massive sulfide deposit: Geophysical Monograph Series, v. 188, p. 321–367.
- Franklin, J.M., Gibson, H.L., Jonasson, I.R., and Galley, A.G., 2005, Volcanogenic massive sulfide deposits: Economic Geology 100th Anniversary Volume, p. 523–560.
- Fuchs, S., Hannington, M.D., and Petersen, S., 2019, Divining gold in seafloor polymetallic massive sulfide systems: Mineralium Deposita, v. 54, p. 789–890
- Gallant, R.M., and Von Damm, K.L., 2006, Geochemical controls on hydrothermal fluids from the Kairei and Edmond vent fields, 23°–25°S, Central Indian Ridge: Geochemistry, Geophysics, Geosystems, v. 7, article Q06018.
- Glemser, O., Haeseler, R.V., and Müller, A., 1964, Gasförmige hydroxide. VII. Uber gasförmiges TeO(OH)<sub>2</sub>: Zeitschrift für anorganische und allgemeine Chemie, v. 329, p. 51–55.

- Glemser, O., Muller, A., and Schwarzkopf, H., 1965, Uber die reaktion von TeO<sub>2</sub> mit wasserdampf bei hoheren drucken und temperaturen: Naturwissenschaften, v. 52, p. 129–130.
- ——1966, Über die reaktion von TeO<sub>2</sub> und CrO<sub>3</sub> mit wasserdampf bei höheren drucken, *in* Ripan, R., ed., Omagiu acad. prof. Raluca Ripan: Bucharest, Editura Academiei Republicii Socialiste România, p. 253–262.
- Goldfarb, R.J., Hofstra, A.H., and Simmons, S.F., 2016, Critical elements in Carlin, epithermal, and orogenic gold deposits: Reviews in Economic Geology, v. 18, p. 217–244.
- Goldfarb, R.J., Berger, B.R., George, M.W., and Seal, R.R., II, 2017, Tellurium: U.S. Geological Survey, Professional Paper 1802, R1–R27.
- Grundler, P.V., Brugger, J., Etschmann, B.E., Helm, L., Liu, W., Spry, P.G., Tian, Y., Testemale, D., and Pring, A., 2013, Speciation of aqueous tellurium(IV) in hydrothermal solutions and vapors, and the role of oxidized tellurium species in Te transport and gold deposition: Geochimica et Cosmochimica Acta, v. 120, p. 298–325.
- Gysi, A.P., 2017, Numerical simulations of CO<sub>2</sub> sequestration in basaltic rock formations: Challenges for optimizing mineral-fluid reactions: Pure and Applied Chemistry, v. 89, p. 581–596.
- Gysî, A.P., and Stefánsson, A., 2011, CO<sub>2</sub>-water-basalt interaction. Numerical simulation of low temperature CO<sub>2</sub> sequestration into basalts: Geochimica et Cosmochimica Acta, v. 75, p. 4728–4751.
- ——2012, Experiments and geochemical modeling of CO<sub>2</sub> sequestration during hydrothermal basalt alteration: Chemical Geology, v. 306–307, p. 10–28.
- Gysi, A.P., Hurtig, N.C., Pan, R., Miron, D.G., and Kulik, D.A., 2023, MINES thermodynamic database: New Mexico Bureau of Geology and Mineral Resources, v. 23, doi: 10.58799/mines-tdb.
- Hannington, M.D., 2014, Volcanogenic massive sulfide deposits: Treatise on Geochemistry, v. 13, p. 463–488.
- Hannington, M.D., Petersen, S., Jonasson, I.R., and Franklin, J.M., 1994, Hydrothermal activity and associated mineral deposits on the seafloor: Geological Survey of Canada, Open File Report 2915C, map 1:35,000,000 and CD-ROM.
- Hannington, M.D., Galley, A.G., Herzig, P.M., and Petersen, S., 1998, Comparison of the TAG mound and stockwork complex with Cyprus-type massive sulfide deposits: Proceedings of the Ocean Drilling Program, Scientific Results, v. 158, p. 389–415.
- Hannington, M.D., de Ronde, C.E.J., and Petersen, S., 2005, Sea-floor tectonics and submarine hydrothermal systems: Economic Geology 100<sup>th</sup> Anniversary Volume, p. 111–141.
- Hannington, M., Jamieson, J., Monecke, T., and Petersen, S., 2010, Modern sea-floor massive sulfides and base metal resources: Toward an estimate of global sea-floor massive sulfide potential: Society of Economic Geologists, Special Publication 15, p. 317–338.
- Hannington, M., Hardardóttir, V., Garbe-Schönberg, D., and Brown, K.L., 2016, Gold enrichment in active geothermal systems by accumulating colloidal suspensions: Nature Geoscience, v. 9, p. 299–302.
- Hardardóttir, V., Brown, K.L., Fridriksson, T., Hedenquist, J.W., Hannington, M.D., and Thorhallsson, S., 2009, Metals in deep liquid of the Reykjanes geothermal system, southwest Iceland: Implications for the composition of seafloor black smoker fluids: Geology, v. 37, p. 1103–1106.
- Hassan, L.Y., and Roberts, M.P., 2017, Tellurides associated with volcanogenic massive sulfide (VMS) mineralization at Yuinmery and Austin, Western Australia: Ore Geology Reviews, v. 80, p. 352–362.
- Helgeson, H.C., and Kirkham, D.H., 1974, Theoretical prediction of the thermodynamic behavior of aqueous electrolytes at high pressures and temperatures: II. Debye-Hückel parameters for activity coefficients and relative partial molal properties: American Journal of Science, v. 274, p. 1199–1261.
- Helgeson, H.C., Kirkham, D.H., and Flowers, G.C., 1981, Theoretical prediction of the thermodynamic behavior of aqueous electrolytes at high pressures and temperatures: IV. Calculation of activity coefficients, osmotic coefficients, and apparent molal and standard and relative partial molal properties to 600°C and 5 kb: American Journal of Science, v. 281, p. 1249–1516.
- Johnson, J.W., Oelkers, E.H., and Helgeson, H.C., 1992, Supcrt92 a software package for calculating the standard molal thermodynamic properties of minerals, gases, aqueous species, and reactions from 1 bar to 5000 bar and 0 °C to 1000 °C: Computers & Geosciences, v. 18, p. 899–947.
- Iizasa, K., Yuasa, M., and Yokota, S., 1992, Mineralogy and geochemistry of volcanogenic sulfides from the Myojinsho submarine caldera, the Shichito-Iwojima Ridge, Izu Ogasawara Arc, northwestern Pacific: Marine Geology, v. 108, p. 39–58.

Iizasa, K., Asada, A., Mizuno, K., Katase, F., Lee, S., Kojima, M., and Ogawa, N., 2019, Native gold and gold-rich sulfide deposits in a submarine basaltic caldera, Higashi-Aogashima hydrothermal field, Izu-Ogasawara frontal arc, Japan: Mineralium Deposita, v. 54, p. 117–132.

- Keith, M., Haase, K.M., Klemd, R., Krumm, S., and Strauss, H., 2016, Systematic variations of trace element and sulfur isotope compositions in pyrite with stratigraphic depth in the Skouriotissa volcanic-hosted massive sulfide deposit, Troodos ophiolite, Cyprus: Chemical Geology, v. 423, p. 7–18.
- Kelley, K.D., and Spry, P.G., 2016, Critical elements in alkaline igneous rockrelated epithermal gold deposits: Reviews in Economic Geology, v. 18, p. 195–216.
- Koschinsky, A., Garbe-Schönberg, D., Sander, S., Schmidt, K., Gennerich, H.H., and Strauss, H., 2008, Hydrothermal venting at pressure-temperature conditions above the critical point of seawater, 5°S on the Mid-Atlantic Ridge: Geology, v. 36, p. 615–618.
- Ridge: Geology, v. 36, p. 615–618.

  Kulik, D.A., Wagner, T., Dmytrieva, S.V., Kosakowski, G., Hingerl, F.F., Chudnenko, K.V., and Berner, U.R., 2013, GEM-Selektor geochemical modeling package: Revised algorithm and GEMS3K numerical kernel for coupled simulation codes: Computational Geosciences, v. 17, p. 1–24.
- Latimer, W.M., 1938, The oxidation states of the elements and their potentials in aqueous solutions: New York, Prentice-Hall, 392 p.
- Lein, A.Y., Cherkashev, G.A., Ul'yanov, A.A., Ul'yanova, N.V., Stepanova, T.V., Sagalevich, A.M., Bogdanov, Y.A., Gurvich, E.G., and Torokhov, M.P., 2003, Mineralogy and geochemistry of sulfide ores from the Logatchev-2 and Rainbow fields: Similar and distinctive features: Geochemistry International, v. 41, p. 271–294.
- Liu, W., and McPhail, D.C., 2005, Thermodynamic properties of copper chloride complexes and copper transport in magmatic-hydrothermal solutions: Chemical Geology, v. 221, p. 21–39.
- Majzlan, J., Notz, S., Haase, P., Kamitsos, E.I., Tagiara, N.S., and Dachs, E., 2022, Thermodynamic properties of tellurite  $(β-TeO_2)$ , paratellurite  $(α-TeO_2)$ ,  $TeO_2$  glass, and Te(IV) phases with stoichiometry  $M_2Te_3O_8$ ,  $MTe_6O_{13}$ ,  $MTe_2O_5$  ( $M^{2*}$ = Co, Cu, Mg, Mn, Ni, Zn): Geochemistry, v. 82, article 125915.
- Marcus, Y., 2018, Do doubly charged monatomicanions exist in aqueous solutions?: Archives of Organic and Inorganic Chemical Sciences, v. 2, 134.
- Martin, A.J., McDonald, I., MacLeod, C.J., Prichard, H.M., and McFall, K., 2018, Extreme enrichment of selenium in the Apliki Cyprus-type VMS deposit, Troodos, Cyprus: Mineralogical Magazine, v. 82, p. 697–724.
- Martin, A.J., Keith, M., Parvaz, D.B., McDonald, I., Boyce, A.J., McFall, K.A., Jenkin, G.R.T., Strauss, H., and MacLeod, C.J., 2020, Effects of magmatic volatile influx in mafic VMS hydrothermal systems: Evidence from the Troodos ophiolite, Cyprus: Chemical Geology, v. 531, article 119325.
- Maslennikov, V.V., Maslennikova, S.P., Large, R.R., and Danyushevsky, L.V., 2009, Study of trace element zonation in vent chimneys from the Silurian Yaman-Kasy volcanic-hosted massive sulfide deposit (southern Urals, Russia) using laser ablation-inductively coupled plasma mass spectrometry (LA-ICPMS): Economic Geology, v. 104, p. 1111–1141.
- Maslennikov, V.V., Maslennikova, S.P., Large, R.R., Danyushevsky, L.V., Herrington, R.J., and Stanley, C.J., 2013, Tellurium-bearing minerals in zoned sulfide chimneys from Cu-Zn massive sulfide deposits of the Urals, Russia: Mineralogy and Petrology, v. 107, p. 67–99.
- Maslennikov, V.V., Maslennikova, S.P., Large, R.R., Danyushevsky, L.V., Herrington, R.J., Ayupova, N.R., Zaykov, V.V., Lein A.Y., Tseluyko, A.S., Melekestseva I.Y., and Tessalina, S.G., 2017, Chimneys in Paleozoic massive sulfide mounds of the Urals VMS deposits: Mineral and trace element comparison with modern black, gray, white and clear smokers: Ore Geology Reviews, v. 85, p. 64–106.
- McDonough, W.F., and Sun, S.S, 1995, The composition of the Earth: Chemical Geology, v. 120, p. 223–253.
- McPhail, D.C., 1995, Thermodynamic properties of aqueous tellurium species between 25 and 350°C: Geochimica et Cosmochimica Acta, v. 59, p. 851–866.
- Mei, Y., Sherman, D.M., Liu, W., Etschmann, B., Testemale, D., and Brugger, J., 2015, Zinc complexation in chloride-rich hydrothermal fluids (25–600°C): A thermodynamic model derived from *ab initio* molecular dynamics: Geochimica et Cosmochimica Acta, v. 150, p. 265–284.
- Mélekestseva, I.Y., Maslennikov, V.V., Tret'yakov, G.A., Nimis, P., Beltenev, V.E., Rozhdestvenskaya, I.I., Maslennikova, S.P., Belogub, E.V., Danyushevsky, L., Large, R., Yuminov, A.M., and Sadykov, S.A., 2017, Goldand silver-rich massive sulfides from the Semenov-2 hydrothermal field, 13°31.13'N, Mid-Atlantic Ridge: A case of magmatic contribution?: Economic Geology, v. 112, p. 741–773.

- Millero, F.J., 1977, Thermodynamic models for the state of metal ions in seawater, in Goldberg, E.D., O'Brien, J.J., McCave, I.N., and Steele, J.H., eds., The global coastal ocean: Multiscale interdisciplinary processes, v. 6, Marine modeling: New York, Wiley, p. 653–693.
- Millero, F.J., Feistel, R., Wright, D.G., and McDougall, T.J., 2008, The composition of standard seawater and the definition of the reference-composition salinity scale: Deep-Sea Research Part I: Oceanographic Research Papers, v. 55, p. 50–72.
- Monecke, T., Petersen, S., Hannington, M.D., Grant, H., and Samson, I.M., 2016, The minor element endowment of modern sea-floor massive sulfides and comparison with deposits hosted in ancient volcanic successions: Reviews in Economic Geology, v. 18, p. 245–306.
- Nordfeldt, P., Allen, R.L., Pitcairn, I.K., and Gibson, H.L., 2019, Topaz-rich breccias at the 1.9 Ga Kankberg Au-Te deposit, Skellefte district, Sweden [ext. abs.]: Biennial SGA meeting, 15th, Glasgow, Scotland, 2019, Proceedings, v. 4, 1868–1871.
- Novoselov, K.A., Belogub, E.V., Zaykov, V.V., and Yakovleva, V.A., 2006, Silver sulfotellurides from volcanic-hosted massive sulfide deposits in the southern Urals: Mineralogy and Petrology, v. 87, p. 327–349.
- Panson, A.J., 1963, Polarography of the ditelluride ion: The Journal of Physical Chemistry, v. 67, p. 2177–2180.
- Pertlik, F., 2001, Vulcanite, CuTe: Hydrothermal synthesis and crystal structure refinement: Mineralogy and Petrology, v. 71, p. 149–154.
- Pierre, S., Gysi, A.P., and Monecke, T., 2018, Fluid chemistry of mid-ocean ridge hydrothermal vents: A comparison between numerical modeling and vent geochemical data: Geofluids, v. 2018, article 1389379.
- Pilote, J.L., Piercey, S.J., Brueckner, S.M., and Grant, D., 2016, Resolving the relative timing of Au enrichment in volcanogenic massive sulfide deposits using scanning electron microscopy-mineral liberation analyzer: Empirical evidence from the Ming deposit, Newfoundland, Canada: Economic Geology, v. 111, p. 1495–1508.
- Quigley, P.O., 2016, The spectrum of ore deposit types, their alteration and volcanic setting in the Penokean volcanic belt, Great Lakes Region, USA: M.S. thesis, Golden, Colorado, Colorado School of Mines, 96 p.
- Reeves, E.P., Seewald, J.S., Saccocia, P., Bach, W., Craddock, P.R., Shanks, W.C., Sylva, S.P., Walsh, E., Pichler, T., and Rosner, M., 2011, Geochemistry of hydrothermal fluids from the PACMANUS, Northeast Pual and Vienna Woods hydrothermal fields, Manus basin, Papua New Guinea: Geochimica et Cosmochimica Acta, v. 75, p. 1088–1123.
- Reithmayer, K., Steurer, W., Schulz, H., and de Boer, J.L., 1993, Highpressure single-crystal structure study on calaverite, AuTe<sub>2</sub>: Acta Crystallographica, v. B49, p. 6–11.
- Robie, R.A., and Hemingway, B.S., 1995, Thermodynamic properties of minerals and related substances at 298.15 K and 1 bar ( $10^5$  Pascals) pressure and at higher temperatures: U.S. Geological Survey Bulletin, v. 2131, 461 p.
- Robinson, R.A., and Stokes, R.H., 1968, Electrolyte solutions: The measurement and interpretation of conductance, chemical potential and diffusion in solutions of simple electrolytes, 2nd ed.: London, Butterworth, 571 p.
- Robie, R.A., Bethke, P.M., and Beardsley, K.M., 1967, Selected X-ray crystal-lographic data, molar volumes, and densities of minerals and related substances: U.S. Geological Survey Bulletin, v. 1248, 87 p.
- Schuyler Anderson, C., 2018, Selenium and tellurium (advance release): U.S. Geological Survey, Minerals Yearbook 2018, p. 65.1–65.8.
- Shock, E.L., and Helgeson, H.C., 1988, Calculation of the thermodynamic and transport properties of aqueous species at high pressures and temperatures: Correlation algorithms for ionic species and equation of state predictions to 5 kb and 1000°C: Geochimica et Cosmochimica Acta, v. 52, p. 2009–2036.
- Shock, E.L., Oelkers, E.H., Johnson, J.W., Sverjensky, D.A., and Helgeson, H.C., 1992, Calculation of the thermodynamic properties of aqueous species at high pressures and temperatures. Effective electrostatic radii, dissociation constants and standard partial molal properties to 1000°C and 5 kbar: Journal of the Chemical Society, Faraday Transactions, v. 88, p. 803–826.
- Shock, E.L., Sassani, D.C., Willis, M., and Sverjensky, D.A., 1997, Inorganic species in geologic fluids: Correlations among standard molal thermodynamic properties of aqueous ions and hydroxide complexes: Geochimica et Cosmochimica Acta, v. 61, p. 907–950.
- Simmons, S.F., and Brown, K.L., 2006, Gold in magmatic hydrothermal solutions and the rapid formation of a giant ore deposit: Science, v. 314, p. 288–291.
- Simmons, S.F., Brown, K.L., and Tutolo, B.M., 2016, Hydrothermal transport of Ag, Au, Cu, Pb, Te, Zn, and other metals and metalloids in New Zealand

geothermal systems: Spatial patterns, fluid-mineral equilibria, and implications for epithermal mineralization: Economic Geology, v. 111, p. 589–618. Stefánsson, A., and Seward, T.M., 2003a, The hydrolysis of gold(I) in aqueous solutions to 600°C and 1500 bar: Geochimica et Cosmochimica Acta, v. 67, p. 1677–1688.

2003b, Stability of chloridogold(I) complexes in aqueous solutions from 300 to 600°C and from 500 to 1800 bar: Geochimica et Cosmochimica Acta, v. 67, p. 4559–4576.

Sverjensky, D.A., Shock, E.L., and Helgeson, H.C., 1997, Prediction of the thermodynamic properties of aqueous metal complexes to 1000°C and 5 kb: Geochimica et Cosmochimica Acta, v. 61, p. 1359–1412.

Tanger, J.C., IV, and Helgeson, H.C., 1988, Calculation of the thermodynamic and transport properties of aqueous species at high pressures and temperatures: Revised equations of state for the standard partial molal properties of ions and electrolytes: American Journal of Science, v. 288, p. 19–98.

Törmänen, T.O., and Koski, R.A., 2005, Gold enrichment and the Bi-Au association in pyrrhotite-rich massive sulfide deposits, Escanaba trough, southern Gorda Ridge: Economic Geology, v. 100, p. 1135–1150.

Tseluyko, A.S., Maslennikov, V.V., Ayupova, N.R., Maslennikova, S.P., and Danyushevsky, L.V., 2019, Tellurium-bearing mineralization in clastic ores at the Yubileynoe copper massive sulfide deposit (Southern Urals): Geology of Ore Deposits, v. 61, p. 133–161.

Vikentyev, I.V., 2006, Precious metal and telluride mineralogy of large volcanic-hosted massive sulfide deposits in the Urals: Mineralogy and Petrology, v. 87, p. 305–326.

Von Damm, K.L., 1990, Seafloor hydrothermal activity: Black smoker chemistry and chimneys: Annual Review of Earth and Planetary Sciences, v. 18, p. 173–204.

Von Damm, K.L., Bray, A.M., Buttermore, L.G., and Oosting, S.E., 1998, The geochemical controls on vent fluids from the Lucky Strike vent field, Mid-Atlantic Ridge: Earth and Planetary Science Letters, v. 160, p. 521–536.

Von Damm, K.L., Lilley, M.D., Shanks, I.C., III, Brockington, M., Bray, A.M., O'Grady, K.M., Olson, E., Graham, A., Proskurowski, G., and the SouEPR Science Party, 2003, Extraordinary phase separation and segregation in vent fluids from the southern East Pacific Rise: Earth and Planetary Science Letters, v. 206, p. 365–378.

Wagner, T., Kulik, D.A., Hingerl, F.F., and Dmytrieva, S.V., 2012, GEM-Selektor geochemical modeling package: TSolMod library and data interface for multicomponent phase models: Canadian Mineralogist, v. 50, p. 1173–1195.

Woodruff, L.G., Attig, J.W., Cannon, W.F., Nicholson, S.W., and Schulz, K., 2003, Geochemistry of bedrock and glacial deposits in the vicinity of the Bend massive sulfide deposit, north central Wisconsin: U.S. Geological Survey, Open-File Report, v. 03-353, 8 p. Nicole Hurtig is an assistant professor of geochemistry in the Department of Earth and Environmental Science at New Mexico Tech (NMT). Her research focuses on hydro/geothermal fluids, ore deposits, trace metal systematics in petroleum systems, and metal transport in hydrothermal fluids. She received her Ph.D. degree in 2014 from



McGill University. Her dissertation focused on metal solubility in vapor-like fluids and active geothermal systems. Thereafter, she was a postdoctoral fellow with the AIRIE Program at Colorado State University for four years. Prior to starting her position at NMT in 2020, Nicole was a research assistant professor at Colorado School of Mines.

Alexander Gysi is an economic geologist in the New Mexico Bureau of Geology and Mineral Resources and an associate professor in the Department of Earth & Environmental Science at the New Mexico Institute of Mining and Technology, USA. He established the Ore Deposits and Critical Minerals Laboratory and maintains the MINES



thermodynamic database for simulating ore-forming processes and fluid-rock interaction. His background includes laboratory experiments, thermodynamic modeling, and work in natural systems to study the behavior of rare earth elements (REEs) and other critical minerals. His expertise includes petrology and mineralogy, aqueous geochemistry, and economic geology. He earned his Ph.D. degree in 2011 from the University of Iceland, part of the Carbfix project on CO2 sequestration into basalts. Between 2011 and 2014 he was a postdoctoral fellow at McGill University in Montreal, Canada, where he studied REE mineral deposits in geologic systems. Between 2014 and 2020, he was an assistant professor at Colorado School of Mines in Golden, Colorado.